UNIVERSITY OF CALIFORNIA SAN DIEGO

Artificial Cornea Modeling for the Validation of a Novel Intraocular Pressure Measurement Device

A thesis submitted in partial satisfaction of the
requirements for the degree Master of Science

in

Engineering Sciences (Mechanical Engineering)

by

Avinash Laha

Committee in charge:

Professor Frank Talke, Chair
Professor Shengqiang Cai
Professor James Friend
Professor Marko Lubarda

2023

The thesis of Avinash Laha is approved, and it is acceptable in quality and form for publication on microfilm and electronically.

University of California San Diego

2023

DEDICATION

To Ma, Baba, and Anushka.
Without your unrelenting love, support, and prayers,
it would be impossible for me to be where I am today.

To all my friends I have had the good fortune of crossing paths with in San Diego.
You will always be an integral part of all I have achieved in these few years.

I also dedicate my work to Abhishek and Vineetha Nigam.
Your never-ending support and well-wishes have made it possible
for me to achieve my academic aspirations thus far.

EPIGRAPH

You can't cross the sea
merely by standing and
staring at the water.

Rabindranath Tagore

TABLE OF CONTENTS

LIST OF FIGURES

LIST OF TABLES

ACKNOWLEDGEMENTS

I would like to thank Professor Frank E. Talke for all his guidance and support throughout my time at the university. His love for knowledge and research to further the field of medical devices has never failed to inspire my own work, and will stay with me beyond these few years.

I would like to thank Dr. Gerrit Melles for imparting his medical knowledge of ophthalmology and supporting our research endeavors. His guidance has been crucial in our attempts to improve existing medical device technology.

I would like to thank Professor Karcher Morris and Matthew Kohanfars. Without their enthusiasm and mentorship, my journey in this arena of research would not have begun.

I would also like to thank the rest of the researchers at the Talke Biomedical Device Laboratory. Their hardwork, collaboration, and friendship have been crucial to my growth and success.

Chapter 2, in part, has been accepted for publication of the material as it may appear in Micromechatronics for Information and Precision Equipment (JAMDSM), 2022. Schwinn, Philip; Laha, Avinash; Melles, Gerrit; Talke, Frank E., JSME/ASME, 2023. The thesis author was a researcher and co-author of this paper.

Chapters 3, 4, and 5, in part, have been accepted for publication of the material as it may appear in Information Storage and Processing Systems, 2023. Laha, Avinash; Srinath, Aravind; Talke, Frank E., ASME, 2023. The thesis author was a researcher and co-author of this paper.

VITA

2020-2021	Undergraduate Research Volunteer, Cardiac Mechanics Research Group
2021	Undergraduate Research Assistant, Center for Memory and Recording Research
2021	Bachelor of Science in Mechanical Engineering, University of California San Diego
2021-2023	Graduate Research Assistant, Center for Memory and Recording Research
2021-2023	Teaching Assistant, University of California San Diego
2023	Master of Science in Mechanical Engineering, University of California San Diego

ABSTRACT OF THE THESIS

Artificial Cornea Modeling for the Validation of a Novel Intraocular Pressure Measurement Device

by

Avinash Laha

Master of Science in Engineering Sciences (Mechanical Engineering)

University of California San Diego, 2023

Professor Frank Talke, Chair

Today, glaucoma is the leading cause of irreversible blindness in the world. Its highest risk factor is related to an elevated intraocular pressure (IOP) within the eye that can cause stress on the optic nerve and deteriorate the visual field in patients. Regular IOP monitoring can be crucial in detecting early onset of glaucoma, especially since surgical cures might not exist in the later stages. To improve the prospect of self-examining ophthalmic devices, we have developed

a handheld 3-in-1 device consisting of 3 commonly used glaucoma screening instruments. This includes a compact slit lamp biomicroscope, visual acuity tester, and a non-contact tonometer. The aim of this device is to enable easy self-examination of the eye more frequently, especially for patients physically unable to travel to in-person clinic appointments to perform them.

To validate the tonometer measurement principle, this thesis investigates the development of an artificial cornea using silicone materials to study corneal deflection as a function of the IOP. Samples were fabricated using 2-part 3D-printed molds that accurately capture the geometry of the human cornea. Young's moduli for a range of selected silicones were evaluated and compared with that of human cornea as well. Eye pressure was simulated using a water-filled manometer channel and readings were obtained from both a commercial and the 3-in-1 device's tonometer to test the designed artificial corneas. Results from both devices validate the use of such a phantom eye apparatus to test similar ophthalmic instrumentation before clinical testing on humans.

Chapter 1

Background

1.1 Introduction to Glaucoma

Degeneration of retinal ganglion cells in the human eye can be a result of elevated intraocular pressure (IOP) which causes damage to the optic nerve [1]. In a healthy eye, aqueous humor production is channeled into the anterior chamber and drained through trabecular and uveoscleral outflows at a constant rate [2]. However, any blockage to this drainage channel or overproduction of aqueous humor can cause fluid buildup within the eye which results in an increased internal pressure. High levels of IOP within the eye can cause cell death in the retinal ganglion network and cause physical damage to the optic nerve, resulting in a set of eye diseases called glaucoma [3]. This can be visualized as shown in Figure 1.1. Since the retinal ganglion cells, their axons, and optic nerve are responsible for relaying visual information to the brain, any damage to them can lead to gradual and irreversible visual field loss [4].

Glaucoma can be subdivided into primary and secondary glaucoma as well as open-angle versus angle-closure glaucoma. Primary Open-Angle Glaucoma (POAG) is associated with a gradual increase in IOP and is the most common form of the disease, followed by Primary Angle-Closure Glaucoma associated with a closure of the anterior chamber angle and sudden IOP change [7]. Today, these diseases are the number one cause of irreversible blindness worldwide. As of 2020, around 57.5 million people are affected by POAG out of a total of 76 million affected by some form of glaucoma-related neuropathy. This number is projected to increase to 111.8

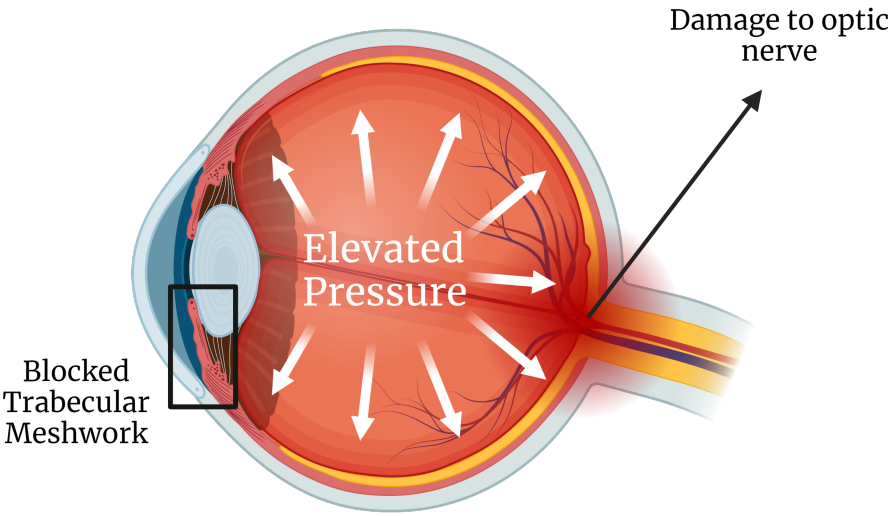

Figure 1.1. Elevated eye pressure causing optic nerve damage in glaucomatous eye [5].

Figure 1.2. Progression of vision field deterioration due to glaucoma. (a) Healthy vision, (b) slight progression with some blindspots, and (c) extreme loss of peripheral vision [6].

million by the year 2040 [8]. Patients developing glaucoma may slowly develop vision defects and "blindspots" in their peripheral vision (Fig. 1.2) which can cause difficulty in performing common day-to-day tasks like walking, reading, facial recognition, and driving. However, gradual onset of glaucoma as seen commonly in POAG is not easily self-detected and can often go undiagnosed until extremely late stages when options for a cure may not even be possible [6]. Individuals aged between 40-80 are also at a higher risk due to age-related diseases, while those younger might develop rarer cases of glaucoma mainly due to genetics and family history [8].

Comprehensive ophthalmic examinations have thus been developed by organizations such as the American Academy of Ophthalmology to focus on testing physical signs as well as patient and family history to screen for glaucoma and other ocular diseases [9]. These examinations include:

- Visual acuity screening with visual field assessment
- External eye examination
- Pupillary function and responsiveness to light
- Ocular alignment and motility
- Slit lamp biomicroscopic assessment
- Intraocular pressure measurement
- Fundus examination
- Assessment of patient's physical and mental health
- Patient's family history of glaucoma or other systemic disease

Similar procedures of routine ocular health screening have been adopted by other developing countries as well [10]. However, an increased IOP remains the most significant risk factor in most types of glaucoma-related diseases. Therefore, early detection using intraocular pressure measurements to ensure normal pressure levels can be imperative in preventing visual field loss and progression of glaucoma [11]. Moreover, diagnosed patients are required to regularly monitor IOP during and after surgery since more aggressive treatment may be required if major eye pressure fluctuations are observed [12].

1.2 Brief History on Tonometry

Today, a device known as the "tonometer" is used to measure intraocular pressure in a patient's eyes. However, ophthalmologists since the early 1800's have attempted to incorporate medical training to manually gauge eye pressure before the advent of such a device. Sir William was one of the first to popularize digital palpation tonometry, or the estimation of ocular tension using finger-massaging techniques [13]. In fact, when early mechanical devices such as indentation tonometers were first introduced in the late 1800's, ophthalmologists still preferred using manual techniques. This changed with the advent of the Schiotz tonometer which enabled cornea indentation using a plunger loaded with varying weights. The IOP value could be calculated using the depth of the corneal indentation created [14]. Although it is not used anymore due to errors associated with varying ocular rigidity, improper positioning, and high measurement variability, it was the gold standard at the time for being relatively inexpensive, easy to use, and did not require extensive ophthalmological training.

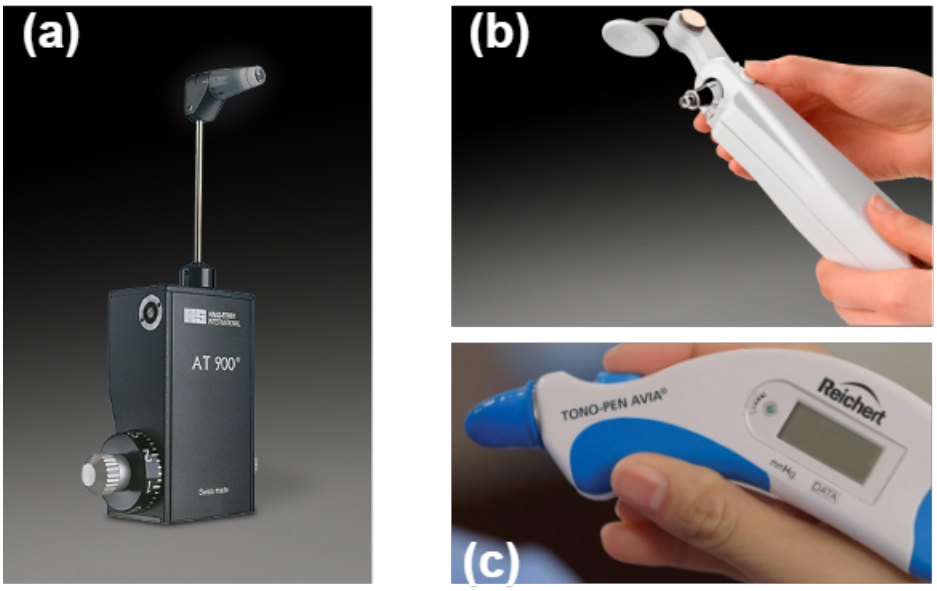

Figure 1.3. (a) Goldmann Applanation Tonometer (HAAG-STREIT AT 900) [15], (b) Perkins Tonometer (HAAG-STREIT MK3) [16], and (c) Tono-Pen Avia (Reichert) [17].

The drawbacks of indentation tonometry were addressed with the invention of the Goldmann Applanation Tonometer (GAT) in 1948 and was based on the Imbert-Fick Law (Fig. 1.3a). This technique is based on the assumption that the intraocular pressure is equal to the force required to flatten a predetermined surface area on the cornea [18]. GAT gained its popularity due to its ease of use, accuracy, and reproducibility, and continues to be the gold standard for IOP measurement in clinics today [14]. However, it needs to be mounted on a slit lamp, is tested with patients in an upright position, and requires the application of local anesthetic. This makes it unideal for rapid repeated use, patients suffering from physical affliction, or those allergic to anesthesia. Moreover, it also slightly deviates from true IOP values since it can be influenced by corneal thickness and biomechanical parameters [19]. Handheld devices such as Perkins (Fig. 1.3b) and Tono-Pen (Fig. 1.3c) tonometers have sought to provide a more portable alternative that can be tested in the supine position and are equipped with disposable latex caps. Yet, they are also significantly affected by corneal thickness variation and high inaccuracy at high IOP values as seen in most glaucomatous eyes [14].

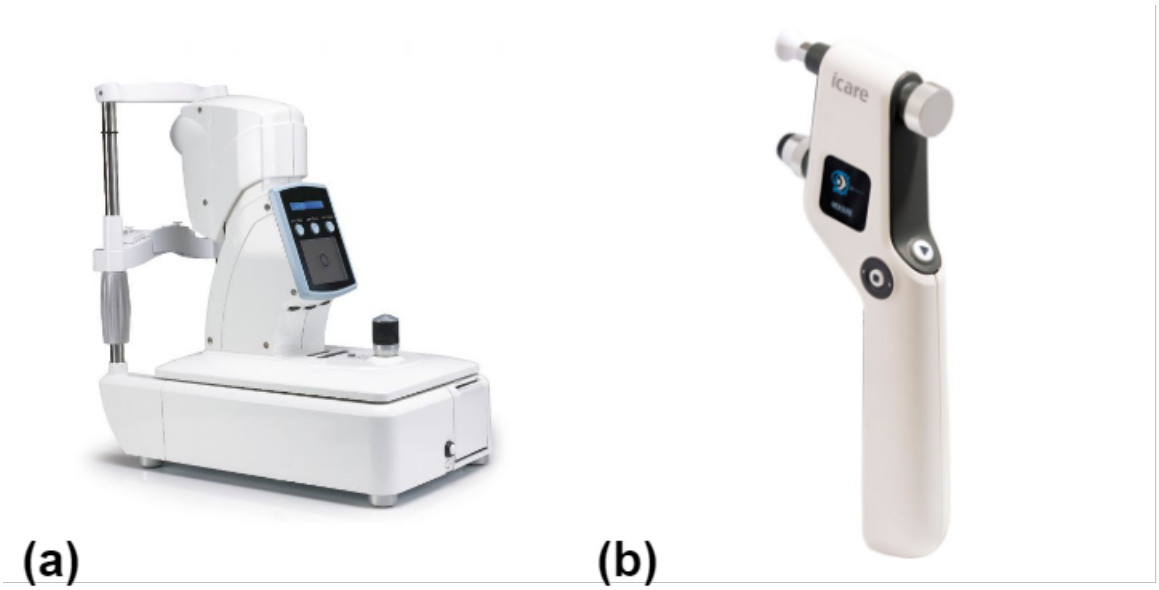

Figure 1.4. (a) Keeler Pulsair Desktop Non-Contact Tonometer [20], (b) iCare IC100 Rebound Tonometer [21].

The development of Non-Contact Tonometry (NCT) offered a more minimally invasive approach than the traditional contact applanation methods. First introduced by Grolman in the 1970s, these devices use an air jet puff to applanate the cornea and do not require an anesthetic, which reduces the risk of infection between successive tests on patients [22]. These systems are usually table-mounted where patients can rest their chin and forehead on the device in an upright position. While a nozzle applies an air pulse at the center of the corneal surface, a collimated beam of light is reflected off cornea onto a sensor tracking the intensity of light reflected over the course of the jet application [23]. When the cornea is fully applanated, the reduction in corneal curvature results in a maximum value of light reflected and detected by the sensor. The air pressure value at this point in time is recorded which enables the calculation of the intraocular pressure value [24]. Advanced iterations of these devices are still used in clinics to this day, such as the Keeler Pulsair (Fig. 1.4a), thanks to their user-friendly and non-contact nature. However, they can be inaccurate at higher IOP values, are highly variable between different devices, and need regular calibration [14].

Another recent innovation that has been a useful alternative to GAT is the rebound tonometer - a handheld device which senses the speed and movement of a tiny probe rebounding off the corneal surface to derive the IOP. These are highly portable, repeatable, and are extremely easy to use without any medical training [14]. In recent studies, the most popular rebound tonometer, iCare IC100 (Fig. 1.4b) has been shown to be comparable to Perkins and GAT tonometry, but underestimate IOP at high pressures [25]. Yet, these measurements can be reliable at low and moderate intraocular pressures, and are an attractive alternative especially in younger or older patients who cannot commute to clinics regularly, or those allergic to anesthetic applications.

1.3 Need for Portable Self-Examining Tonometers

Both non-contact and contact techniques used in commercial tonometers have had various levels of success in providing helpful information about the internal eye pressure. In modern clinics, Goldmann Applanation Tonometers and Non-Contact Tonometers are most commonly used due to their high accuracy and reliability [26]. However, most of these desktop instruments are bulky, expensive, and require the presence of a physician or operator to function properly. For these reasons, they are traditionally found only at clinics where they can be used under appropriate medical supervision [14]. This makes it difficult to carry out regular tests on patients that need to physically travel to the clinic even for such routine exams. This can also be impractical for patients who may suffer from other physical complications that prevent them from frequently traveling to a clinic. Additional office visits add to transportation costs and medical bills which may lead to unnecessary financial burden to patients, especially in low-income households [8]. This situation has become further apparent over the recent Coronavirus pandemic, when lockdowns made it even more difficult to perform in-person eye check-ups and follow-up exams on patients [27].

Thus, there has been a widespread interest in developing portable, handheld ophthalmic devices that can perform similar tests as the ones available in eye clinics from the comfort of one's home. The rise in "teleophthalmology" which describes the practice of performing comprehensive ophthalmic exams virtually on a patient has grown in popularity in recent years given the success rate in various countries [8]. Particularly successful in rural areas, studies have shown that the majority of participating patients did not require an in-person visit at all. These tests can be done either synchronously or asynchronously and have proven to be a new viable alternative to time-consuming in-person clinic exams [27].

Thus, various types of handheld tonometers have also been explored to reduce the number of required in-person clinic visits and ensure regular monitoring of intraocular pressure. In addition to previously developed Perkins and Tono-Pen portable devices, handheld NCT instru-

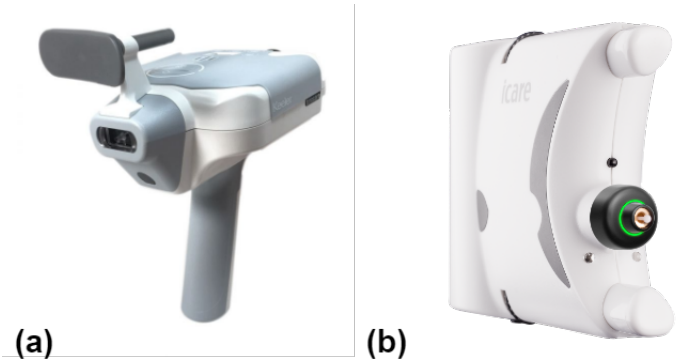

Figure 1.5. (a) Keeler TonoCare handheld NCT [28], (b) iCare Home self-examining rebound tonometer [29].

ments such as the Keeler TonoCare (Fig. 1.5a) and Pulsair IntelliPuff have entered the market as non-contact alternatives to applanation methods. Since IOP has also been shown to fluctuate over the course of the day, devices that allow for self-examination can be key in determining these trends along with success rate of treatment after surgery and/or medication [30]. As a result, the recently introduced iCare Home (Fig. 1.5b) and Home 2 devices have expanded upon previously designed rebound tonometry methods to enable patients to test for IOP themselves, without the need for another operator or licensed physician. In some studies, iCare Home has shown lower variability in measurements than Tono-Pen or IC100 tonometers, and also shows promising results comparable to GAT [31]. These innovations have further opened up avenues for effective intraocular pressure measurements and early glaucoma diagnosis without the need for regular clinic visits.

1.4 Tonometer Testing and Calibration Standards

Even though the field of tonometry has seen major improvements over the past few decades, it is important to note that different types of these devices may prove beneficial only in certain cases. For example, Goldmann Applanation Tonometry is considered the gold standard even now, but it can only be used in clinics since it must be mounted on a desktop slit lamp and the need for a trained operator [22]. Non-contact tonometers might be slightly easier to

use and avoid risks for infection, but are not as accurate as GAT and Perkins tonometry [14]. Additionally, some studies state a decrease in accuracy over time for desktop NCT models and recommend regular calibration [32]. Rebound tonometers provide the easiest process for IOP measurement and have opened up the avenue for commercial self-examination, but are also inaccurate at higher eye pressures and the accuracy can depend on the skill of the operator [25].

Most importantly, the choice of tonometer might affect the accuracy of eye pressure readings obtained by a given patient, which can prove ineffective in glaucoma diagnosis. Some of these devices also use IOP correction algorithms to account for variation in corneal thickness, curvature, and other biomechanical factors between patients [33], [34]. These "adjusted" eye pressure algorithms vary in accuracy and are often not easily disclosed as they are part of confidential company information, making it very difficult to obtain a standardized reading to compare between different devices [35]. Therefore, there is an existing need to develop a calibration standard for tonometers. Results obtained from newly developed devices must be compared to existing ones to ensure reliability in intraocular pressure measurements for all patients.

While testing the efficacy of an IOP-measuring device, it must provide accurate readings at a variety of eye pressures as close as possible to the actual internal eye pressure. Although the normal IOP range for humans exists between 10-21 mmHg, these devices must also be able to register both lower and higher values to successfully indicate extreme pressure fluctuations related to glaucoma [36]. Thus, studies have been conducted to test various types of contact and non-contact tonometers on cadaveric human eyes while being constrained and held at a constant internal fluid pressure [31]. Some research has also utilized excised porcine corneas [37] or even cannulated rabbit and monkey eyes [38] to control the IOP during testing. These cornea samples are most commonly connected to a syringe or manometer channel with known fluid pressure to reliably adjust the internal pressure in experiments. Since GAT is known to be the gold standard for eye pressure measurements today, other NCT or handheld devices are commonly compared to results obtained from a GAT or Perkins tonometer [39], [40] [41]. Studies like these have

been responsible for showing various degrees of accuracy as well as deviation from actual IOP in readings obtained from newer devices.

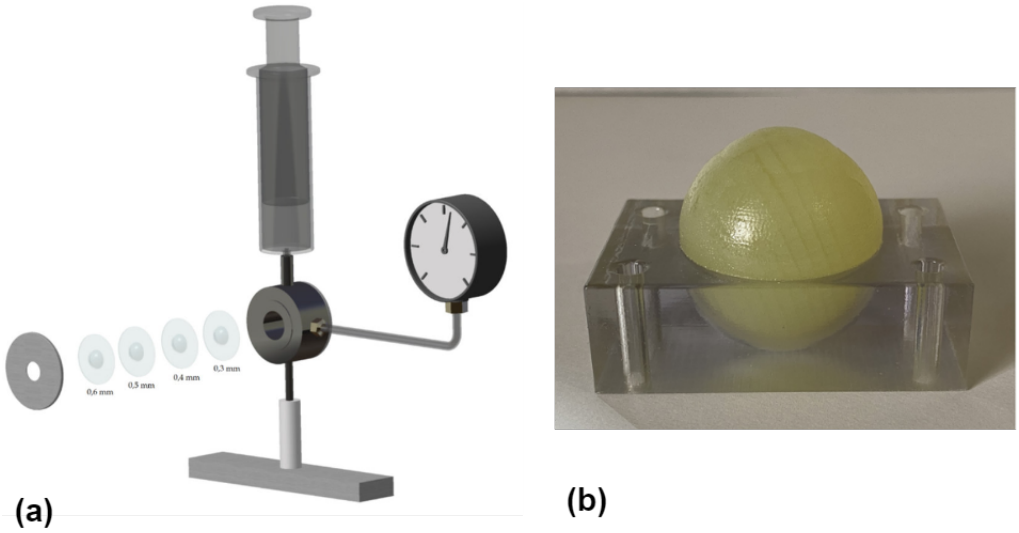

Figure 1.6. (a) Varying thickness in artificial silicone cornea models simulating IOP due to fluid-filled syringe [35], (b) 3D-printed eye globe made with rubber-like material simulation IOP variation by changing corneal thickness [42].

Recently, research has also been performed in artificial cornea models and developing test setups to manually control the dimensions of the cornea being tested while varying the internal eye pressure [35], [43]. Elastomeric materials such as silicone or polydimethylsiloxane (PDMS) are used to fabricate these thin cornea samples since the geometry and mechanical properties can be chosen to reflect those seen in human corneas (Fig. 1.6a). This method also allows for changing the geometry of the artificial cornea to study the IOP measurement variation due to corneal thickness, curvature, and rigidity [35]. 3D-printed phantom eyeball models as shown in Figure 1.6b have also been developed using rubber-like print material filled with gel support material for a portable calibration standard [42]. Instead of using an adjustable fluid channel to simulate a range of IOP levels, this method varies the corneal thickness from 200-800 micrometers to change the readings obtained from a Tono-Pen AVIA instrument. These different methods can be especially useful for not only testing existing devices, but also for calibrating new handheld devices as self-examination and tele-optometry become more popular in practice.

They also circumvent the need to obtain cornea samples from a live specimen or eye bank, which can be much more difficult to obtain. However, the research conducted in artificial cornea modeling for simulating intraocular pressure is fairly novel, and must be expanded upon and further evaluated in future studies.

1.5 Thesis Overview

Previously, the Talke Biomedical Device Laboratory has attempted to develop a handheld ophthalmic device that combines three of the most common ophthalmic instruments: a slit-lamp bio-microscope, a visual acuity screener, and most importantly, a non-contact tonometer to evaluate the overall ocular health of a patient [44]. This device houses all 3 instruments within a portable 3D-printed casing and is equipped with a touchscreen that allows users to perform these examinations and access test results seamlessly by themselves. It is also internet-enabled that allows easy sharing of these results with a trained physician or doctor for further analysis if required. Compared to other existing handheld ophthalmic devices, this device uses a novel approach in combining multiple instruments into one portable form-factor for a wide range of optical tests. As discussed previously, eye pressure fluctuations pose the highest risk factor for progression of glaucoma. Thus, with a focus on the handheld device's tonometer, an artificial cornea model was developed to validate the IOP measurements obtained by it. These cornea samples can be fabricated with silicone elastomeric materials and clamped into an artificial anterior chamber. The intraocular pressure can be simulated and adjusted using a manometer channel filled with water, which is connected to the anterior chamber. This designed apparatus can be used to observe the behavior of an artificial human cornea at different IOP levels and calibrate the handheld tonometer without the need for excised/cannulated human corneas or direct clinical testing which can all be hard to achieve at the prototyping stage for such a device.

This thesis discusses design iterations made on the tonometer instrumentation for the purpose of making the multi-functional ophthalmic device more compact and easy-to-use. This

work focuses on the development of the artificial corneas that can be used as a standard of calibration for handheld tonometers. The method of designing and fabricating these models are explained along with material characterization of the used silicone materials. To ensure validity of the cornea model, inflation tests were performed and compared to a finite element model as well as human corneal behavior seen in existing literature. Additionally, tonometer readings were obtained using an existing commercial tonometer at different simulated intraocular pressure levels. Videos were recorded using the tonometer housed within the handheld multi-functional device at these IOP levels as well, to study different corneal deformation levels observed. The research explored can be used to obtain calibration information for this device and similar tonometers in the future and effectively reduce the need for excised human corneas in a wet lab environment as is common but troublesome in current practice. Future work is also planned on further developing this device to make it more light-weight, user-friendly, and reliable in terms of repeatable measurements. Further development of the artificial corneas using different materials and geometries in addition to testing with other commercial tonometers can also help improve the validation process of such devices.

Chapter 2

Novel Handheld Ophthalmic Device

2.1 Overview of the Device

To address the growing need for self-examination of the eye and expand upon already existing glaucoma diagnostic instruments, a multi-functional handheld 3-in-1 ophthalmic device was developed at the Talke Biomedical Device Lab [44]. This device features compact versions of not just one, but three common eye examinations, specifically a slit lamp biomicroscope, visual acuity screener, and non-contact tonometer (Fig. 2.1). A housing and device lid were designed and 3D-printed using additive manufacturing techniques. Three eye holes with nose-bridge channels placed in between them were designed to allow patients comfort while using the device. A 5-inch touchscreen panel on the farther end of the device also enables the user to navigate through the different functionalities and select which instrument they wish to use. An on-board Raspberry Pi microcontroller functions in tandem with an Arduino UNO board to control the electro-mechanical components of the three instruments and uses the touchscreen as the main user input system. A small air puff-generating system is enclosed on top of the device that consists of a compressed CO_2 regulator and a solenoid valve responsible for generating the air pulses during tonometer testing.

A rechargeable battery connected to a voltage regulator board is placed inside the device and is capable of delivering power to all the instrument components as well as both microcontrollers. A custom-made printed circuit board (PCB) was also designed to efficiently

route the power to all these components. The device also features ports to recharge the battery easily such that a patient would not need to remove the lid and replace the battery or other connections that might tamper with the overall working of the device. A main ON/OFF power button is placed beside the touchscreen panel that turns on the power to the entire device. Vent holes were also placed close to a miniature fan to account for airflow control and avoid any overheating issues with the microcontroller boards residing inside the device.

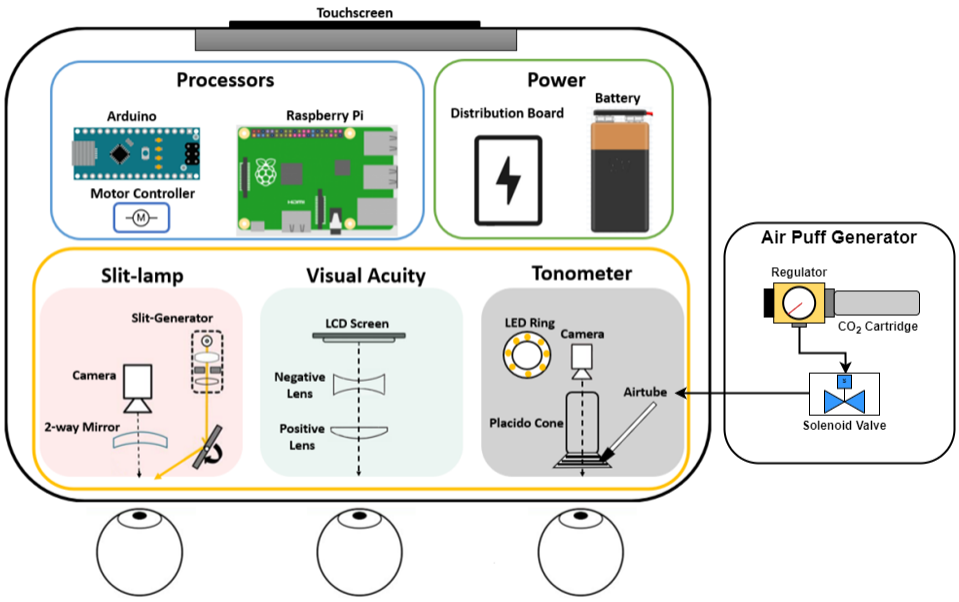

Figure 2.1. Overall schematic of the handheld 3-in-1 device showing all the main components.

The latest prototype is shown in Figure 2.2. The main goal of this device is to facilitate easy self-examination of the eye. It also features internet capabilities so that all test results can be shared with the patient's physician or a specialized doctor in case further analysis is needed. This can be highly effective for those living in remote areas or patients who cannot easily travel to clinics regularly for these routine check-ups. The easy-to-use device also helps monitor intraocular pressure and other eye metrics throughout the course of the day to diagnose any glaucoma-related symptoms originating from IOP fluctuations. The combination of these three eye exams inside one portable device adds to the existing tele-optometry technology today,

and can prove useful in improving remote glaucoma diagnosis. The following subchapters go into detail about the functionality of the three different device instruments.

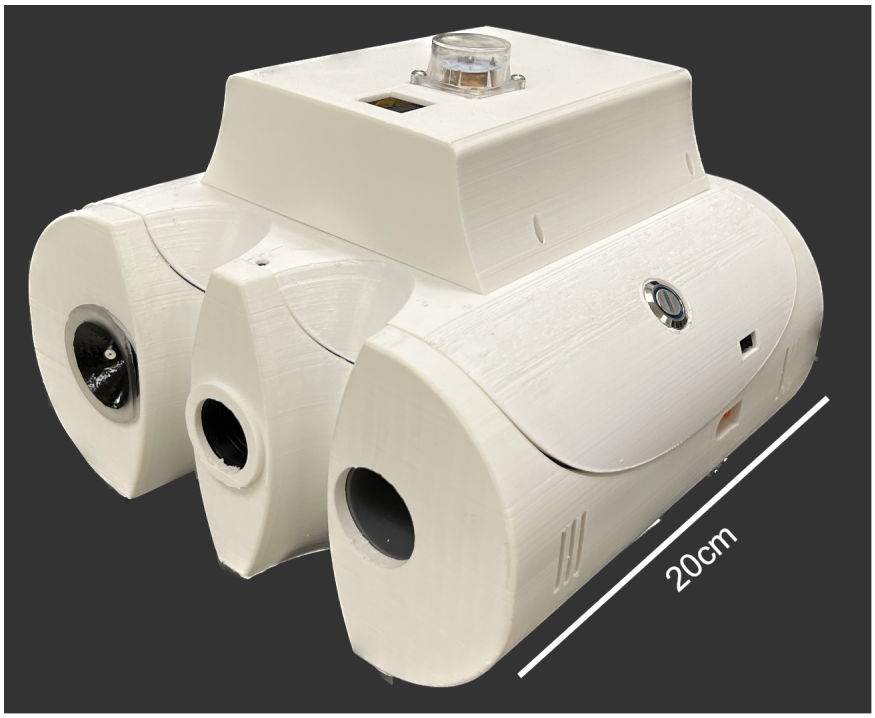

Figure 2.2. 3-in-1 ophthalmic device prototype with three eye holes for the individual glaucoma diagnostic instruments. The compact air-puff-generating box is mounted on top of the lid.

2.2 Slit Lamp Biomicroscope

A slit lamp instrument combines a light source and a microscope to produce a thin beam of light that can be focused onto the eye to study lesions, physical aberrations, or other features of the anterior chamber [45]. While desktop devices continue to be the most commonly used for this examination in clinical practice, some handheld smartphone attachments have also been designed for glaucoma and cataract screening [46]. A similar method was implemented in previous research conducted at the Talke Biomedical Device Lab to incorporate a slit-lamp biomicroscope and a visual acuity screener inside a “2-in-1” device for self-examination [47]. The components implemented within the current 3-in-1 prototype heavily draw from the success of this technique.

The beam of light is generated using a high-intensity LED which is connected to a heatsink to avoid overheating. The produced light is focused into a thin rectangular beam using a collector lens, 3D-printed slit component, and an objective lens. All of these components are collectively placed inside a 3D-printed casing and form a "slit-generator" module. The light generated using this module is focused onto a rotating mirror mounted on a stepper motor shaft, which redirects the beam onto the user's eye through one of the device's eyeholes. The Raspberry Pi controls the movement of the stepper motor shaft, which automatically sweeps the beam of light from one corner of the patient's eye to the other, in an attempt to visualize any abnormalities much like conventional slit lamp bio-microscopes. A camera module placed in front of the eyehole records a video of the eye during the sweeping mechanism so that it can be reviewed by the patient or a doctor at a later time. A two-way mirror is also present in front of the camera to allow patients to self-align their eye during the procedure and also effectively reduces the focal length of the camera. The components for the slit-lamp are shown in Figure 2.3.

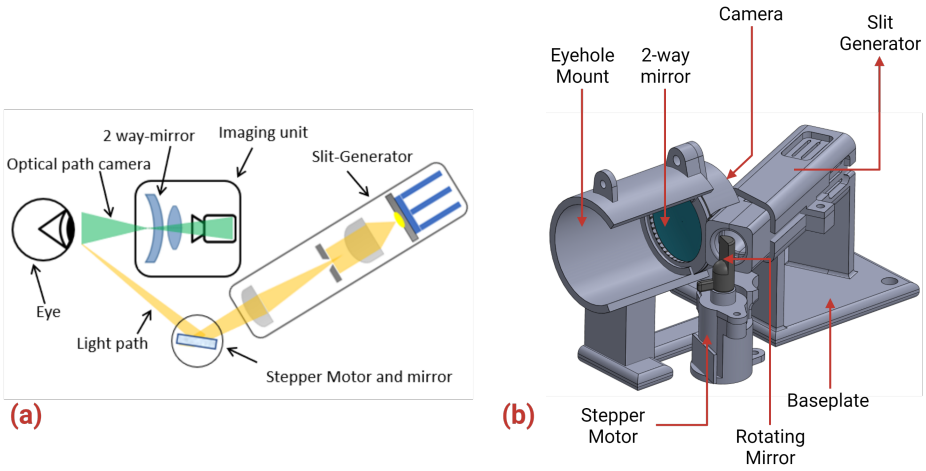

Figure 2.3. Slit lamp microscope components. (a) Design schematic and ray diagram, (b) CAD subassembly with mounts for all components.

2.3 Visual Acuity Screener

Another important method in measuring a patient's ocular health is through the visual acuity test that measures the eye's ability to recognize letters at different orientations and sizes at a distance of 20 feet away [48]. Many "optotypes", or letters and figures have been developed to test visual acuity since the mid-1700s, with the tumbling 'C' or 'E' being simple yet effective enough for these tests [49]. Many handheld devices and smartphone attachments have been introduced that use this tumbling optotype method for patients to self-examine for visual acuity [50]. The previously developed 2-in-1 device at the Talke Medical Device Lab also utilized a similar tumbling E visual acuity tester where separate buttons were used to determine the perceived orientation of the optotype during the test [47].

The visual acuity screener inside the novel 3-in-1 device consists of a 1.3-inch LED screen to display the optotypes. An optical system magnifies the projected letters to appear as would be seen 20-feet away in a clinical version of the exam. To achieve this, a positive lens projects the image farther away from the physical placement of the screen inside the 3-in-1 device, and a negative lens reduces the magnification to the appropriate scale before the optotypes are projected through the positive lens (Fig. 2.4).

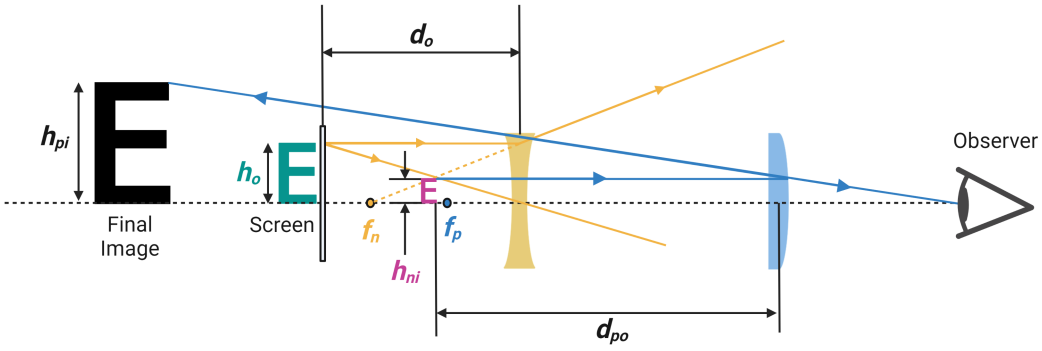

Figure 2.4. Ray diagram of the visual acuity optical system [5].

$$h_{ni} = h_o \times \frac{-f_n}{d_o - f_n} \tag{2.1}$$

$$h_{pi} = h_{ni} \times \frac{-f_p}{d_{po} - f_p} \tag{2.2}$$

The placement of these lenses are determined by a combination of the thin lens and magnification equations and the resulting image height can be calculated as given by Equations 2.1 and 2.2 [44]. First, the height of the interim virtual image (h_{ni}) formed by the negative lens is calculated based upon the focal length (f_n) and distance (d_o) of the lens from the screen. This image height is then used to calculate the final desired image height (f_{pi}) using the focal length (f_p) and placement (d_{po}) of the positive lens. Since the desired image heights, h_{po} are given by standard visual acuity charts, the size of the optotypes to be projected on the screen (h_o) can be determined.

A cylindrical lens holder is used to place the positive and negative lenses at the appropriate distances and mounted in place between the LED screen and the device's eyehole (Fig. 2.5). The test spans 8 levels ranging from 20/200 to 20/20 visual acuity, and each level corresponds to a pair of left and right-facing "E" letters. At each level, one of these letters are displayed on the screen and the user is prompted to determine its orientation. Two buttons (left and right) housed on the lid of the device are connected to the Raspberry Pi system and can be used by the patient to select the orientation of the displayed optotype. After receiving input from the buttons, the screen automatically projects the next randomized figure. If the orientation of more than 3 out of 5 displayed letters at a certain level are correctly selected, the test's algorithm changes visual acuity level to show letters of the next smaller size. On the contrary, if more than 2 out of 5 letters are incorrectly chosen, the test moves up a level and shows letters of a larger size. This continues until the user selects at least 4 letters correctly at the current size level, and the resulting visual acuity level is then displayed on the touchscreen on the other end of the device. If the smallest size level is reached, the resulting visual acuity would be 20/20 corresponding to normal healthy vision.

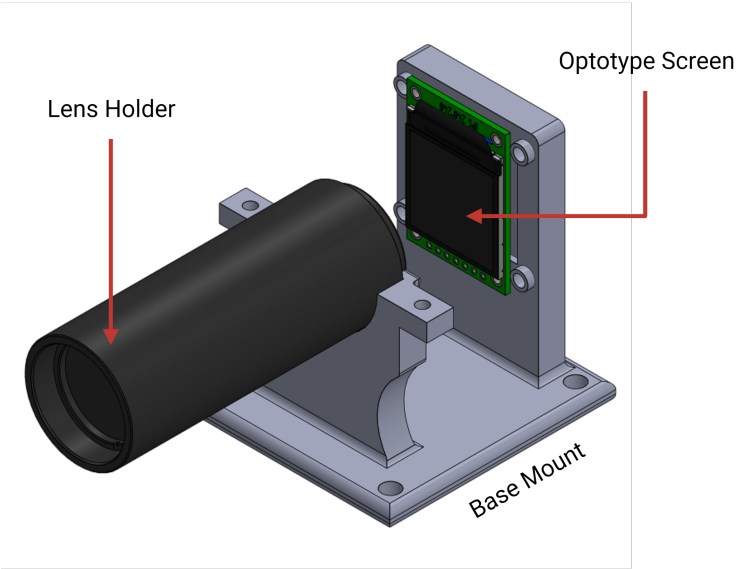

Figure 2.5. Main optical components of the visual acuity screener.

2.4 Non-Contact Tonometer

As previously discussed in Chapter 1, high intraocular pressure can be a major risk factor for the progression of glaucoma in patients. Therefore, the developed 3-in-1 device incorporates existing non-contact tonometry methods to help measure IOP values during self-examination of the eye. Common commercial NCT's use a pulse of air exerted onto the corneal surface for a short amount of time to initiate deformation. The handheld device's tonometer also uses an air puff onto the cornea that is provided by a pressurized air regulator with a compressed CO_2 cartridge. Tubing connects the outlet from this regulator to a common "input" channel on a miniature 2-way solenoid controlled by the Arduino in the device. One of the two outlet channels remains sealed, while the other is connected to a nozzle designed to deliver the produced air puff onto the eye. When the test is initiated, the Arduino's algorithm switches the solenoid channels, activating the output channel to the nozzle for a brief period of 100 milliseconds to deliver a short puff. The pressure of this puff is manually controlled using the dial of the air regulator, and is maintained around 5 psi or 260 mmHg. The tested cornea is thus applanated under this pressure during which a video needs to be recorded to observe the corneal mechanical response. Three

consecutive puffs are generated using this system with 2 second gaps in between to observe any major variation in corneal deformation under the same conditions.

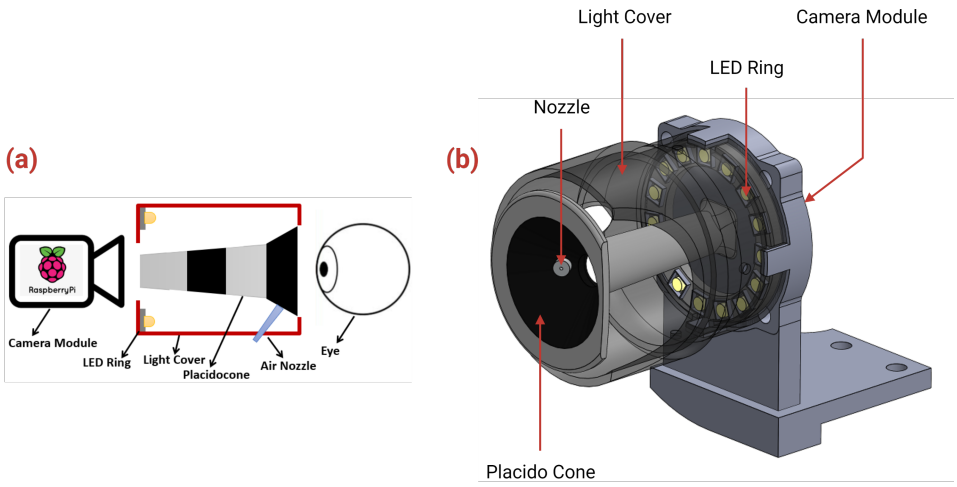

Figure 2.6. Non-contact tonometer (a) schematic and (b) CAD subassembly (light cover made translucent for clarity).

Various optical sensing techniques like high-speed Scheimpflug cameras or infrared sensors are used in commercial devices to document the corneal response to this air puff force and draw conclusions about the IOP [51], [24]. The tonometer within the 3-in-1 device uses somewhat of a different principle in sensing corneal deformation using a camera directly in line with the device's eyehole. Between the eyehole and camera is a Placido cone with a pair of painted rings (Placido rings), which are projected onto the cornea with the help of an LED ring placed behind the cone (Fig. 2.6). The Placido ring projection technique is most commonly utilized in corneal topography assessment using keratometry, where these sets of concentric rings being projected onto the patient's eye can give visual information of the anterior segment [52]. The LED ring in the 3-in-1 device is turned on during the tonometry test to project the Placido cones before, during, and after the cornea is applanated due to the short air puffs. The camera records a video at 120 FPS (frames per second) to provide 12 frames showing a fully applanated cornea during each 100-millisecond air puff. The goal with this test is to observe the displacement and deformation of these projected rings when applanation occurs. Since the

degree of deformation is dependent on the resistive forces provided by the eye pressure, the video can be analyzed to calculate IOP levels seen during the test.

2.5 Prototype Development

Manufacturing the handheld 3-in-1 device was achieved using rapid prototyping and design-for-manufacturability considerations in mind. The first step focused on designing a schematic to obtain a form factor suitable to house all needed components for the three instruments (Fig. 2.1). Previous models of similar handheld devices developed in the Talke Biomedical Device Lab were studied to expand on the existing research [53], [54]. The main housing was designed such that all components for the slit lamp, visual acuity, and tonometer fit safely within the bottom case. Additionally, extra space was also designed to fit the Raspberry Pi microprocessor, user touchscreen, and all needed connections for the components. The lid for the bottom housing was designed to encase the rechargeable battery, the Arduino, and voltage regulation board. All these electro-mechanical components were designed, imported, and assembled in a SolidWorks model as shown in Figure 2.7(a). Next, the designed goggle-shape housing with compatible lid were 3D-printed with polylactic acid filament (PLA) using fused deposition modeling (FDM) printing techniques. This printing method was chosen for a bigger build platform and obtaining a prototype in under 24 hours. All electronic components were then acquired and assembled with the appropriately designed mounts. These mounts were also designed as SolidWorks parts and printed using stereolithography (SLA) techniques for greater resolution at smaller dimensions.

The assembled components could then be wired and/or soldered to the voltage regulator for power distribution and the microcontrollers to enable full functionality of these instruments (Fig. 2.7b). In early prototypes, the entire electronic system within the bottom housing was connected in parallel with the output port of the voltage regulator to allow an equal 5V voltage to all components. This daisy chain was later replaced with a custom PCB that efficiently distributes the power to multiple components connected in parallel like before. This reduces the volume of

wired connections thereby decluttering the interior section of the device. Better wire management also allows for decreased risk of power failure, short circuits, and loose connections within the housing.

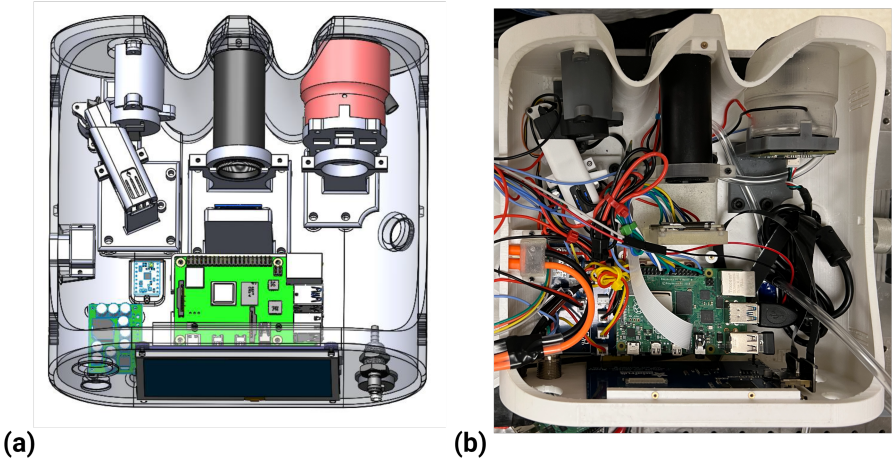

Figure 2.7. The 3-in-1 device's (a) CAD model and (b) prototype with 3D-printed parts and electro-mechanical components assembled.

With the components correctly wired, the lid was safely secured using designed clips as well as screw holes on top of the bottom housing. Apart from all interior components, the device also requires an air puff generating system to enable proper functioning of the tonometer system. In earlier models, this was achieved using a mechanical piston activated by a motor and gear train (Fig. 2.8). The last gear has teeth only on half of its periphery, and is able to pull back the assembled spring and release it after a half-revolution. The spring is then released from tension such that the attached piston slams the inner chamber forcing an air pulse through the nozzle. This entire mechanism was then placed inside a custom rectangular box containing a fan, a power source, and required connections to the Arduino for proper functionality of the tonometer [44]. However, this box measures almost as wide as the housing of the 3-in-1 device and thus, needs to be connected to the main housing externally. This eventually hinders the goal of making this device easy to use for self-examination without the aid of an operator, as multiple connected boxes make it difficult to perform handheld tests with the device.

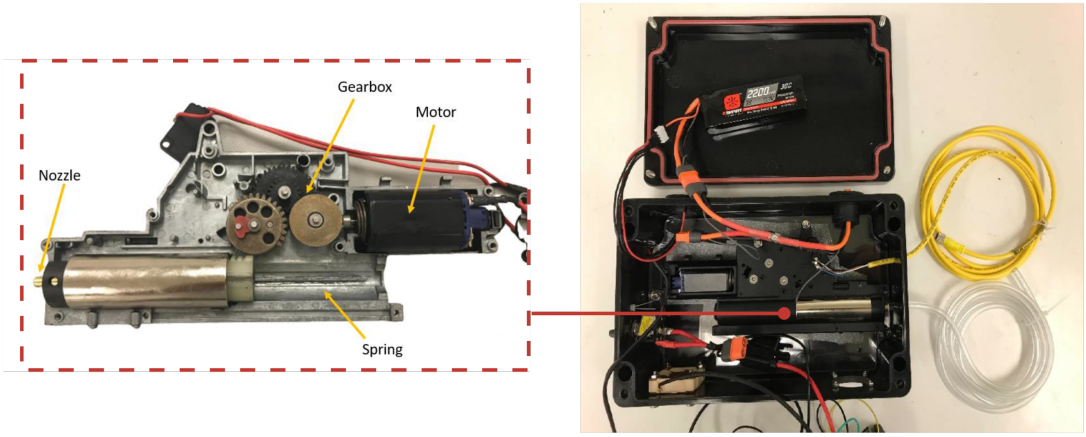

Figure 2.8. Older air puff generator box with mechanical piston mechanism.

A more compact solution was implemented in the most recent prototype, with the design of the smaller air puff generator casing that can easily be attached to the lid of the device. Instead of using a piston mechanism, a mini air regulator and compressed CO_2 cartridge was used to generate the air pulse. The knob on top of the air regulator can be used to manually set the desired pressure for the air puff, which is displayed on the attached gauge. This also provides a more reliable way of adjusting the puff pressure as opposed to replacing the spring inside the piston mechanism which would also require additional troubleshooting. Moreover, the piston mechanism creates a much more audible noise while performing the puff, which can be undesirable for patient use. Figure 2.9 shows the designed case for the regulator system that allows easy viewing of the pressure gauge's dial as well as access to the regulating knob and air cartridge once it needs to be replaced.

After assembling the 3D-printed parts, electronic components, and implementing the new PCB and air-puff system, the device is ready for initial performance testing. Python and C++ scripts to control the separate instruments in the device were developed for the Raspberry Pi and Arduino, respectively. These were then uploaded to the processors that allowed users to choose the various tests and internet features of the device via the touchscreen. The developed graphic user interface (GUI) is shown in Figure 2.10. Upon confirming that all components function

as expected, the device can progress into the pre-clinical testing phase. The following chapters discuss in detail the design of artificial eye models that aid in this next phase of validation for the handheld device.

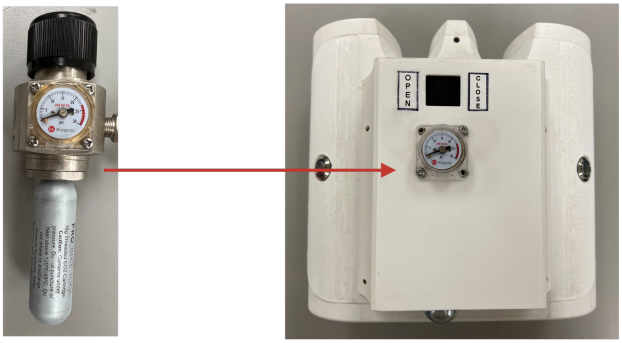

Figure 2.9. New air regulator with cartridge. This assembly sits inside the new generator box mounted on top of the device lid.

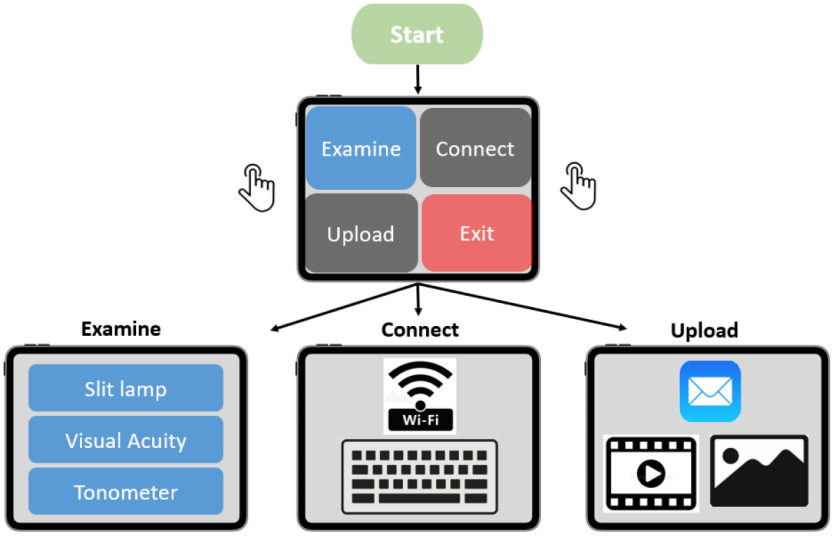

Figure 2.10. Graphic user interface accessible on the touchscreen.

Chapter 2, in part, has been accepted for publication of the material as it may appear in Micromechatronics for Information and Precision Equipment (JAMDSM), 2022. Schwinn, Philip; Laha, Avinash; Melles, Gerrit; Talke, Frank E., JSME/ASME, 2023. The thesis author was a researcher and co-author of this paper.

Chapter 3

Artificial Cornea Model

3.1 Structure of the Human Eye

The human eye consists of several components vital in refracting visual images and relaying them to the brain for a healthy visual field. The cornea is the outermost fibrous tissue that is optically transparent and protects the eye from external germs, debris, and infection. Together with the tear film, it forms the main optical system responsible for refracting and focusing the light entering the eye before it reaches the iris, pupil, and crystalline lens [55]. The entire eye globe is divided into 3 main chambers. The region enclosed by the posterior of the cornea and the anterior of the iris and crystalline lens is known as the anterior chamber, which mainly consists of aqueous humor. The posterior chamber is defined as the region in between the iris, lens, and ciliary body and is also filled with aqueous humor [56]. The third and final chamber of the human eye globe is called the vitreous cavity which lies in between the crystalline lens and the optic nerve. It is mainly composed of vitreous humor, a gel-like fluid that secures the retina in place, and allows light to travel from the lens to the retina and optic nerve [55]. The optic nerve lies at the posterior end of the eye globe, and in conjunction with the photoreceptors, sends visual information to the visual cortex of the brain [57].

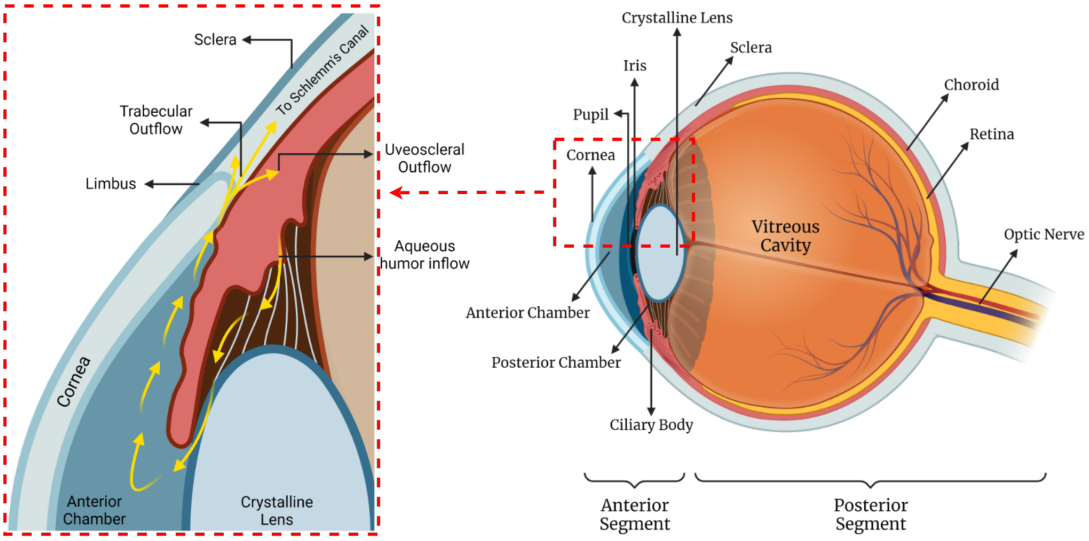

Figure 3.1. Structure of the human eye globe showing parts of the anterior and posterior segments. Magnified section highlights the regulated flow of aqueous humor in the anterior chamber [5].

The overall structure is shown in Figure 3.1. To understand the mechanism of intraocular pressure regulation, it is important to take a closer look at the anterior chamber. Aqueous humor is generated by the ciliary body that creates an inflow of the fluid into this eye chamber. This is circulated throughout the chamber inducing hydrostatic pressure on the posterior surface of the cornea. To prevent excess buildup of aqueous humor, the trabecular meshwork and uveoscleral tissues channel amounts of the fluid out of the anterior chamber [55]. A regular rate of outflow balances the inflow maintaining a regular level of IOP in the eye. Studies indicate that a healthy human eye exhibits IOP values between 10 and 21 mmHg [58]. However, if there is an irregularly high rate of aqueous humor production or blockage in either outflow mechanisms, fluid pressure buildup may occur within the eyeball. Although glaucoma may originate from other types of ocular altercations, an elevated eye pressure is one of the primary risk factors that can cause progression of vision loss in patients.

Thus, it is essential to study the state of the eye, especially the anterior segment at both regular and irregular pressure levels. Since the corneal membrane forms the outer surface of

the anterior chamber, a physical model mimicking the geometry and mechanical properties can provide information about the ocular response to a change in IOP levels. Additionally, such a model should be able to simulate a range of fluid pressures as exhibited by both healthy and glaucomatous eyes to observe changes to an eye model.

3.2 Anatomy of the Cornea

To successfully mimic a human cornea, it is necessary to obtain a model with accurate geometry and mechanical properties as a human eye. The existing literature shows some studies that have been performed to measure various geometrical parameters such as central corneal thickness (CCT), posterior curvature (PC), anterior curvature (AC), etc. Techniques like Optical Coherence Tomography (OCT) and Ultrasound Pachymetry can be used to observe the posterior and anterior segments of the eye and can be extremely helpful in measuring the geometrical dimensions in patients [59], [60]. Chapter 1.1 discusses variance in intraocular pressure readings due to change in certain corneal dimensions. Thus, it is important to accurately define the overall anatomy of the human cornea to ensure consistency in the modeled samples.

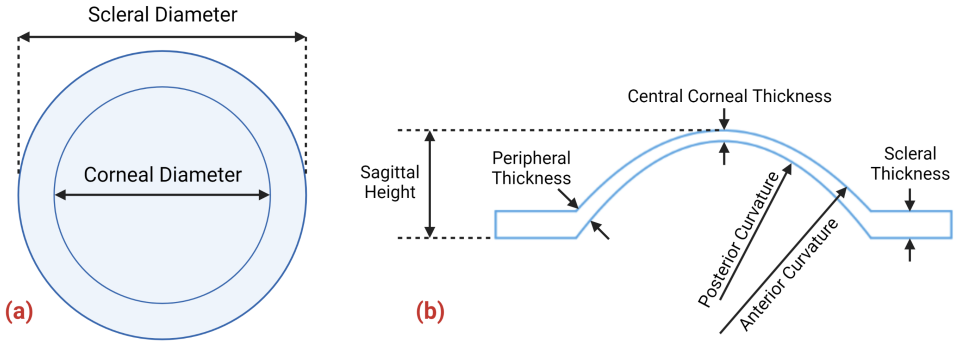

Figure 3.2. Geometrical dimensions of the cornea labeled on the (a) top view and (b) side view.

The cornea and scleral tissue cohesively form the outer surface of the eyeball. The region in between the transparent cornea and opaque sclera is known as the limbus. The average diameter of the cornea is between 10.7 mm and 12.58 mm. The radius of the scleral strip around the base of the cornea has also been observed to be around 11.3 mm [61]. The average scleral

thickness ranges from around 0.4 mm near the central cornea to 1 mm at the posterior region of the eye globe [62]. These parameters are shown in Figure 3.2. Upon observing the cornea from a side view, it can be noticed that it is a convex, aspherical lens. This implies that the anterior curvature (7.8 mm) is different from its posterior curvature (6.5 mm) [59]. In addition to the posterior and anterior curvatures, the cornea is defined by the sagittal height, which is the distance between the apex of corneal curvature and the base where it attaches to the limbus of the eyeball. This value has been studied in OCT instruments as well, and has an average value of 3.74 ± 0.19 mm [63]. The central corneal thickness (CCT) is another important parameter that can vary between patients and may also lead to a variation in intraocular pressure measurement in some commercial tonometers, as discussed in earlier chapters. Ultrasound pachymetry has revealed that the cornea measures thinner at the center with a mean value of 530μm, and thicker at the periphery with a mean value of 705μm [60]. These dimensions are also listed for clarity in the following subchapter in Table 3.1.

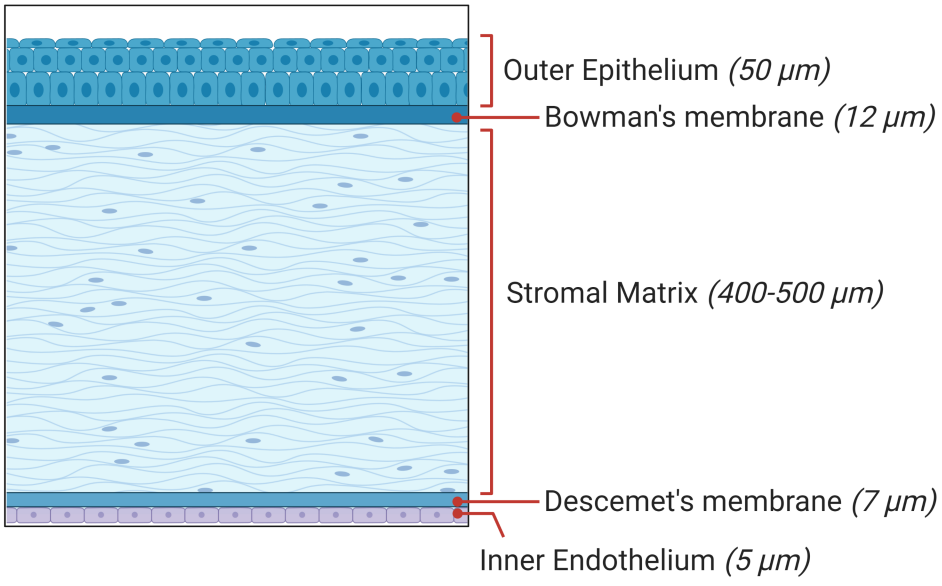

Figure 3.3. Main layers and membranes of the human cornea [5].

In addition to basic geometry, it is important to consider the biomechanical properties of the human cornea while designing an artificial model as well. The human cornea is composed of three major cell layers varying in thickness [59] as shown in Figure 3.3. The outer epithelial cells and inner endothelial layers exhibit a higher in-plane stiffness than the central stroma [64]. To study how this structure contributes to the biomechanical response, a common mechanical testing method known as trephine inflation is used. Here, corneal "buttons" consisting of the cornea attached to a scleral boundary are clamped and inflated using fluid at different pressures to study the apical rise of the cornea. Stress-strain plots can then be obtained in order to derive Young's modulus values at these points [65]. Studies show an initially linear relationship between pressure and corneal displacement, followed by a non-linear rise in displacement starting around 5 kPa or 40 mmHg (Fig. 3.4). This is theorized to be due to the initial stiffness being dominated by the stromal matrix while the non-linear region is a result of collagenous fibers in the endothelium and epithelium becoming taut and contributing to a much higher stiffness [64]. Young's modulus, E, thus increases linearly from 0.2 MPa to 0.7 MPa between 0 mmHg and 80 mmHg posterior pressure, respectively [66].

Other techniques like Scheimpflug imaging using Corvis-ST devices have also been explored to observe corneal response to forces seen in common tonometry methods. These often use the Orssengo-Pye algorithm to calculate the Young's modulus using the area of mechanical applanation in GAT or NCT-based tonometers [67]. Imaging in high-speed cameras like the Corvis-ST record the corneal deflection in response to the applanation. They also provide the added benefit of providing an in-vivo measurement of the Young's modulus, as opposed to other mechanical testing methods. The mean value lies between 0.2-0.3 MPa with a 95% confidence interval ranging from 0.05-0.40 MPa [68], [69].

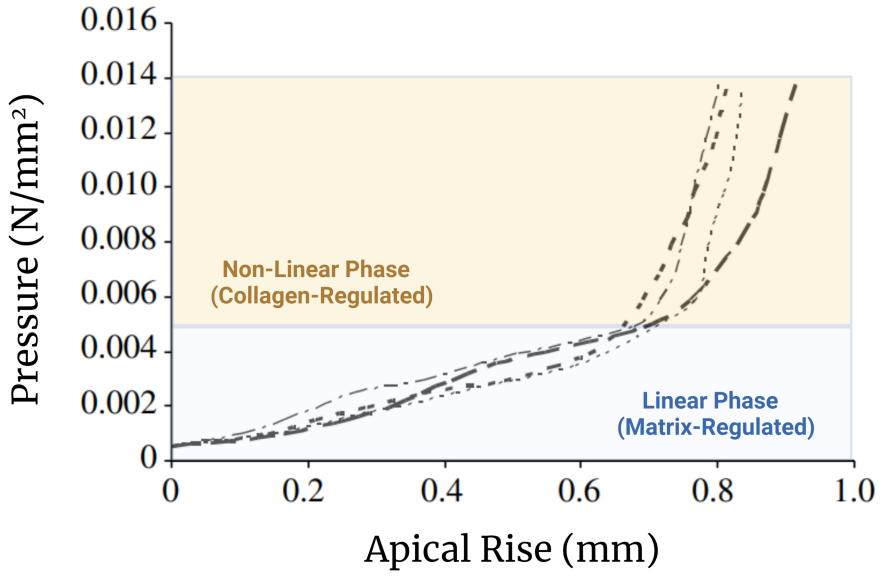

Figure 3.4. Inflation tests showing initial linear phase regulated by stiffness of the stromal matrix followed by a non-linear increase in stiffness due to collagen fiber straightening [64].

3.3 Modeling the Artificial Cornea

The previous subchapters have discussed the importance of capturing not only the geometry but also the mechanical properties such as Young's modulus while designing an artificial cornea model. Considering the most important parameters observed in various OCT studies, a 3D Computer-Aided Design (CAD) model of a cornea with scleral boundary was designed on SolidWorks. To reflect the basic geometry of a human cornea, the values were defined as listed in Table 3.1.

Table 3.1. Geometrical parameters of human cornea compared to the artificial cornea models.

	Human Cornea	**Artificial Cornea**
Diameter (mm)	10.7–12.58	12.3
Central Thickness (mm)	0.48-0.58	0.550
Posterior Curvature (mm)	6.50	6.50
Anterior Curvature (mm)	7.80	7.80

Emphasis was placed on matching the curvature and the thickness variation seen at the center and periphery of a human eye. The sagittal depth was also defined such that the height of the artificial cornea matches the values seen before. A scleral boundary was also designed as part of this model with the intention of providing a region that can be clamped in a test stand during experimentation. This mimics the cornea being constrained by scleral tissue in a human eyeball. These samples essentially result in a corneal button model closely matching those commonly used in trephine inflation tests. Figure 3.5 shows the overall dimensions and the final CAD design of the modeled cornea.

To match the stiffness values observed in existing literature, the fabrication material of choice was a silicone elastomer that exhibits similar Young's modulus values. A range of commercially available silicones were acquired that were stated to have Young's moduli within the range of 0.069-0.15MPa. Tensile tests were additionally performed on coupon samples made with these materials to confirm these values as discussed in detail in Chapter 4. Silicone can also easily be shaped and cured into complex geometries, which can be ideal while manufacturing corneas of tunable dimensions. With the cornea and sclera 3D model designed, it can then be used to design a manufacturable mold that enables easy fabrication of the desired corneal geometry.

3.4 Fabrication Methods

To provide a mold for the silicone cornea sample, a 3D model was created consisting of a top and bottom part detailed with the outer geometry of a human cornea. The top part of the assembly has an indentation in the center that matches the anterior curvature of the cornea. An extruded dome is designed on the bottom mold that accurately models the posterior curvature. A circular region also exists around the base of the posterior end to mimic a thin scleral boundary around the cornea as well. Additionally, four alignment rods were also designed with coinciding holes on the top part to ensure an evenly circular molded sample by preventing any sideways

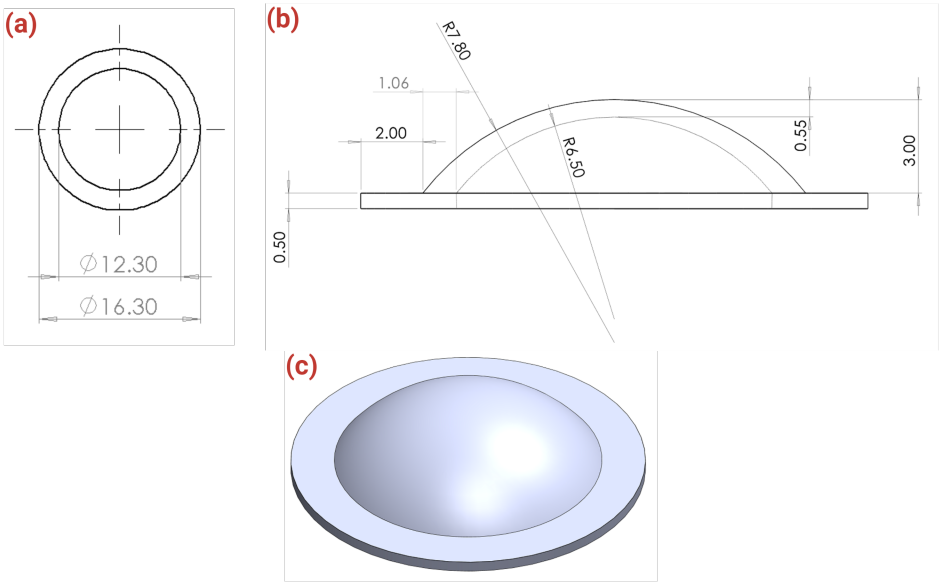

Figure 3.5. Geometry of the designed artificial cornea shown on the (a) top view, (b) side view, and (c) isometric view. All dimensions shown in millimeters.

rotation or movement while clamping. Narrow channels run from the edge of the scleral region to the edge of the bottom mold to allow excess silicone material to drain out while preparing the samples. This allows a safer way of over-filling the mold which can be helpful in avoiding air bubbles and localized cavities in the end product.

3D printing offers easy manufacturing of complex customizable geometries such as the ones needed to mold the artificial cornea samples. Thus, the 2-part mold assembly was printed using a Formlabs 3B+ Stereolithography (SLA) printer using Black [70] and Clear [71] resin. Both materials allow a fine resolution of 25 micrometers during printing, which ensures smooth surfaces for molding posterior and anterior curvatures of the cornea while preserving geometrical detail at the sub-millimeter scale. While Black resin features a higher tensile strength and modulus ensuring a more long-lasting product, printing the molds in Clear resin enables an improved visual aspect to ensure the molds are correctly aligned, clamped, and whether unforeseen air bubbles may have formed. The prints were then cleaned with isopropyl alcohol (IPA) and inserted in an automatic IPA wash for 10 minutes. They were then extracted and left inside an ultraviolet (UV) curing chamber for 30 minutes at 60°C for further strengthening by

UV-induced cross-linking of resin polymer chains. These molds can then be used to cure silicone in the shape of the desired cornea, and can also be reused to create multiple samples after being cleaned with IPA between uses. Figure 3.6 shows the 3D model as well as the printed parts obtained through this process.

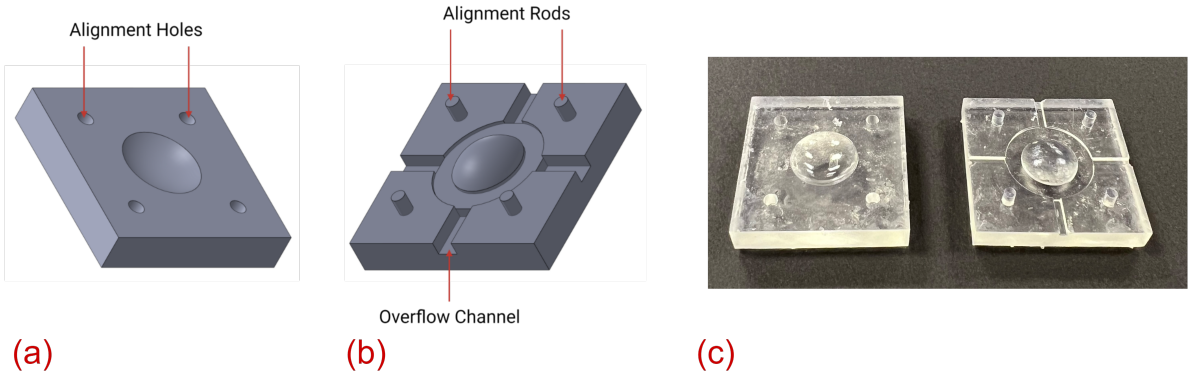

Figure 3.6. 3D CAD model of the (a) top mold, (b) bottom mold, and (c) 3D-printed parts in Formlabs Clear resin.

With the 3D-printed molds prepared, the next step was to pour in the silicone for curing. Different materials of commercially available 2-part curing silicones were chosen which can be combined in a 1:1 weight ratio. After pouring desired weights of parts A and B of the silicone in a mixing cup, they were mixed at room temperature in open air to ensure an even mixture between the two parts. This was then inserted inside a degassing chamber and subjected to a vacuum pressure of 13 psi to remove any bubbles from the mixture before molding begins. After removal from this chamber, the uncured silicone is steadily poured into the cavity of the 3D-printed top mold and enclosed with the bottom mold. This assembly is then clamped and left to cure at room temperature and ambient pressure for over 24 hours. The seal between the top and bottom molds is then gently pushed open with the help of miniature flathead screwdrivers to obtain the resulting silicone-molded corneas. A variety of different silicones having reported Young's moduli in the human corneal range were prepared as shown in Figure 3.7.

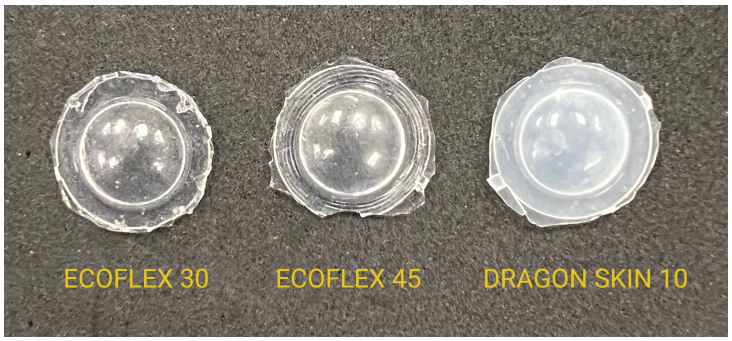

Figure 3.7. Artificial cornea samples fabricated using 3 different silicones of varying stiffness.

It was initially observed that the molded cornea samples do not have a highly reflective surface unlike the clear, transparent human cornea. Although the optical properties do not greatly affect the mechanical response the models attempt in capturing, a reflective outer surface is extremely helpful in clearly projecting the Placido rings with the tonometer system in the handheld 3-in-1 device. Since molded silicone can take up optical shine of the molding surface, the 3D-printed molds were sprayed with a thin coat of reflective acrylic sealant before the molding process. After this layer was allowed to dry for 24 hours, the silicone corneas were molded using the steps outlined as mentioned before. The resulting samples had a visible change in reflectivity and were expected to show a much clearer image of Placido ring projections during performance testing (Fig. 3.8). This process was repeated for all the silicone materials being studied and resulted in a greatly reproducible method of fabrication.

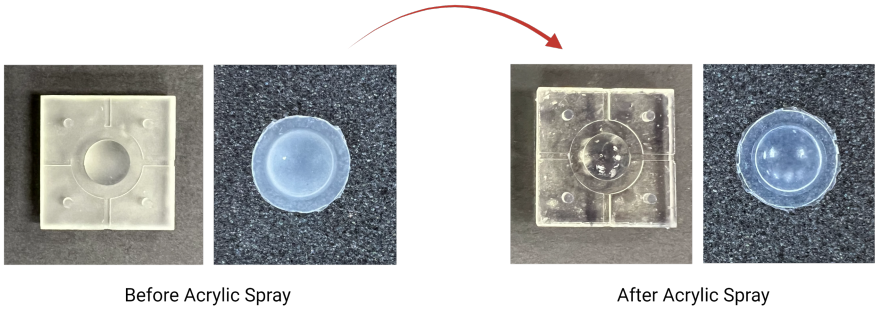

Figure 3.8. 3D-printed mold and resulting cornea reflectivity (a) before and (b) after spraying with acrylic sealant spray.

3.5 Simulation of Intraocular Pressure

Apart from a geometrically and mechanically accurate artificial cornea model, it is crucial to successfully utilize this in simulating changing pressures within the eye. In a healthy human eye, intraocular pressures can vary anywhere between 10 and 21 mmHg [58]. However, any fluctuations dropping below or increasing above this range can be seen in patients suffering from glaucoma-related diseases as discussed in earlier chapters. To enable a reliable method in simulating this variance in eye pressure, a test setup consisting of an anterior chamber and a manometer water channel was prepared. The artificial anterior chamber is commercially obtained from Barron and most commonly used to harvest donor samples or perform tests on excised human corneas. Thus, the dimensions of this chamber are easily compatible with the artificial cornea models designed to mimic such corneal samples.

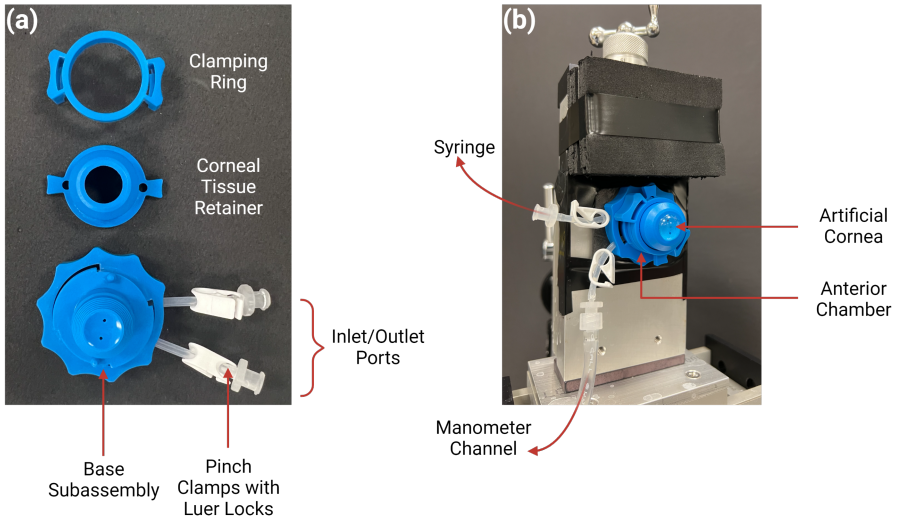

Figure 3.9. Artificial anterior chamber parts (a) disassembled and (b) assembled with the artificial cornea and mounted onto the test stand.

Figure 3.9(a) shows several parts of the chamber that can be used to clamp the artificial samples at the scleral boundary when installed into the setup. This simulates the cornea being constrained at the limbus and connected to the sclera in a human eyeball. This artificial anterior chamber is sealed at the back end and connected to two tube ports. One of these tubes connects

to the water channel (manometer port), while the other (syringe port) can be used to inject or drain fluid from the chamber and manometer. The artificial corneas can then be clamped within the anterior chamber and mounted on a test stand as shown in Figure 3.9(b). The pinch clamp to the syringe port remains closed unless a syringe is being used to change the chamber pressure. The clamp to the manometer channel remains open during testing to ensure the pressure in the chamber matches that in the manometer channel.

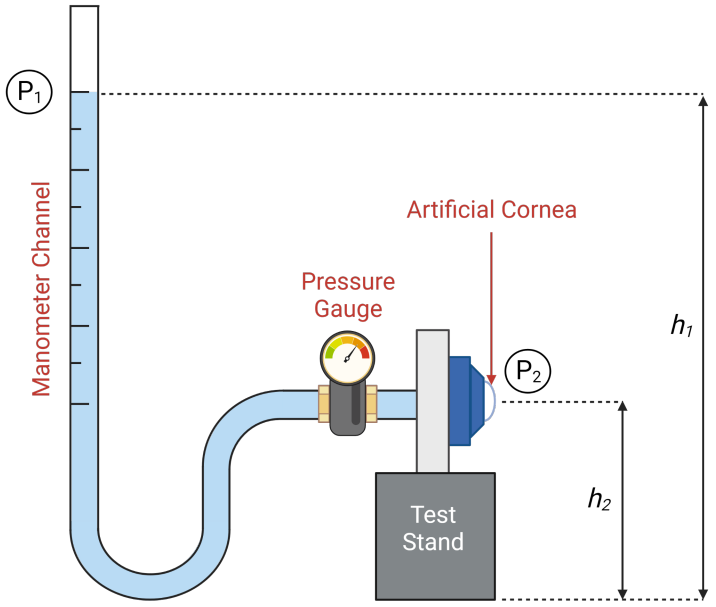

Figure 3.10. Phantom eye model setup showing adjustable manometer channel simulating intraocular pressure onto the clamped artificial cornea [5].

To generate hydrostatic pressure in the anterior chamber, the manometer tube connected to it can be filled with a fluid with known density, such as water in this case. The entire setup is detailed in Figure 3.10. Bernoulli's principle gives a relationship between pressures and fluid velocities at two given heights in a fluid channel and is stated as follows:

$$P_1 + \frac{1}{2}{v_1}^2 + \rho g h_1 = P_2 + \frac{1}{2}{v_2}^2 + \rho g h_2 \tag{3.1}$$

Since the top of the manometer channel is open to the atmosphere, the gage pressure at this point, P_1 is zero. The velocities v_1 and v_2 at points 1 and 2 are also effectively zero since the fluid particles at a given point in time are static in the system. Thus, the pressure at the level of the cornea, P_2 can be derived as a function of the fluid density (ρ), acceleration due to gravity (g), and the difference in the height of fluid in the manometer column (h) as shown in Equation 3.2. The fluid density of water was taken as 1000 kg/m^3 and g was assumed as 9.81 m/s^2. Rearranging this equation, we can derive the vertical distances on the manometer tube that result in a range of pressures simulating different intraocular pressures in the artificial anterior chamber (Eq. 3.3).

$$P_2 = \rho g(h_2 - h_1) = \rho g \Delta h \tag{3.2}$$

$$\Delta h = \frac{P_2}{\rho g} \tag{3.3}$$

A set of manometer channel heights can now be selected to induce hydrostatic pressures simulating low, normal, and high IOP. Thus, markings were made on the manometer tube that corresponded to pressures ranging from 0 mmHg to 40 mmHg as described in Table 3.2. Water was then filled to these heights to simulate these pressure values. To ensure the fluid channel results in accurate levels of pressure at the cornea level, an in-line pressure gauge was mounted at the same height as the clamped cornea, which confirmed the actual pressure values at these water heights.

Table 3.2. Calibration table for manometer channel in the phantom eye setup.

Manometer Pressure (mmHg)	0	10	20	30	40
Column Height, Δh (cm)	0	13.60	27.21	40.81	54.42

Chapter 3, in part, has been accepted for publication of the material as it may appear in Information Storage and Processing Systems, 2023. Laha, Avinash; Srinath, Aravind; Talke, Frank E., ASME, 2023. The thesis author was a researcher and co-author of this paper.

Chapter 4

Mechanical Characterization

4.1 Tensile Coupon Tests

4.1.1 Experimental Setup

To initially select a set of materials to fabricate the artificial cornea models, several commercially available silicones underwent standardized tensile testing. The goal of these experiments was to ensure that Young's modulus values for these materials fall within documented human corneal ranges. One of the most common mechanical testing methods for elastic solids is tensile coupon testing using ASTM D638-14 standards. Using the specified coupon dimensions, a mold was first designed on SolidWorks and later printed using a FormLabs 3B+ SLA printer in Black resin. This was also cleaned with an IPA wash and UV-cured for 30 minutes at 60°C. With the resin mold prepared, tensile coupons were made by pouring mixed silicone into the designed cavity and sealed for 24 hours at room temperature and pressure. Much like the silicone cornea fabrication method, 2-part silicones were mixed in equal weight ratio, and degassed in a vacuum chamber before molding. This process was repeated for various silicone materials - EcoFlex 30 (ECO30), EcoFlex 45 Near Clear (ECO45-NC), and Dragon Skin 10 (DS10). Three coupons were fabricated for each silicone material in preparation for mechanical testing. The fabrication process is highlighted in Figure 4.1.

After extracting these coupons, they were carefully sprayed with dark acrylic paint in order to generate a random speckled pattern on the surface. This is done so that a video can

be recorded during the tensile testing experiment and digital image correlation (DIC) methods can be employed to calculate the elongation by tracking the movement of these speckled dots. The coupons were then clamped using self-tightening grips of a MARK-10 uniaxial tester. A camera was placed securely on a tripod facing the setup to record the elongation of the coupons. The coupons were then pulled at a constant rate of 100 mm/min and the force gauge data was recorded for 1200 data points resulting in a 2 minute video on the camera.

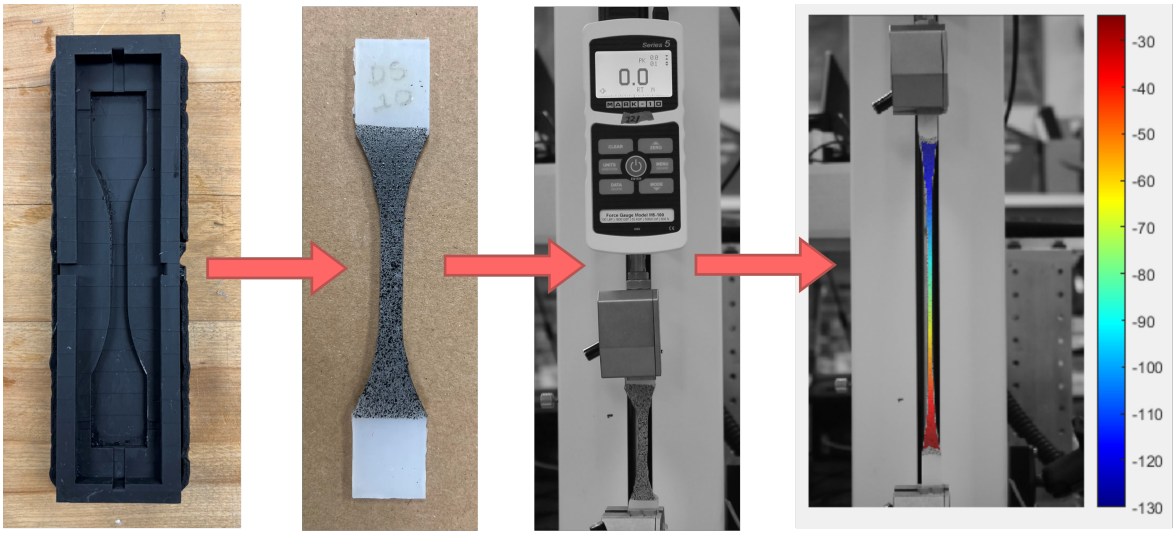

Figure 4.1. Coupon molding and tensile testing process. Pictured left to right: 3D-printed mold; coupon sample with speckled pattern; sample loaded into the uniaxial tester; DIC results in Ncorr_post.

4.1.2 Digital Image Correlation

Using a Python script, the videos were spliced into 1200 frames corresponding to the data points acquired from the uniaxial tester's force gauge. These images were then loaded into a MATLAB DIC-software called Ncorr, that is capable of seed-tracking the sprayed dots on the tensile coupons and obtaining displacement data over the entire video [72]. The results from this program are then imported into Ncorr_post, a post-processing software for Ncorr that calculates strain values from the displacement calculations [73]. This process is also shown in Figure 4.1. The extracted x-direction strain can be used to calculate the change in cross-sectional area (A)

over time. Using these values with the force gauge data (F), the stress values (σ) can be obtained using equation 4.1 below. The stress values can then be plotted with the y-directional strain component obtained from the Ncorr_post program on a stress-strain curve in MATLAB.

$$\sigma = \frac{F}{A} \tag{4.1}$$

4.1.3 Tensile Test Results

The stress-strain curves were obtained for 3 silicone materials - ECO30, ECO45-NC, and DS10 after having undergone uniaxial tensile testing. The compiled results were plotted in MATLAB as shown in Figure 4.2.

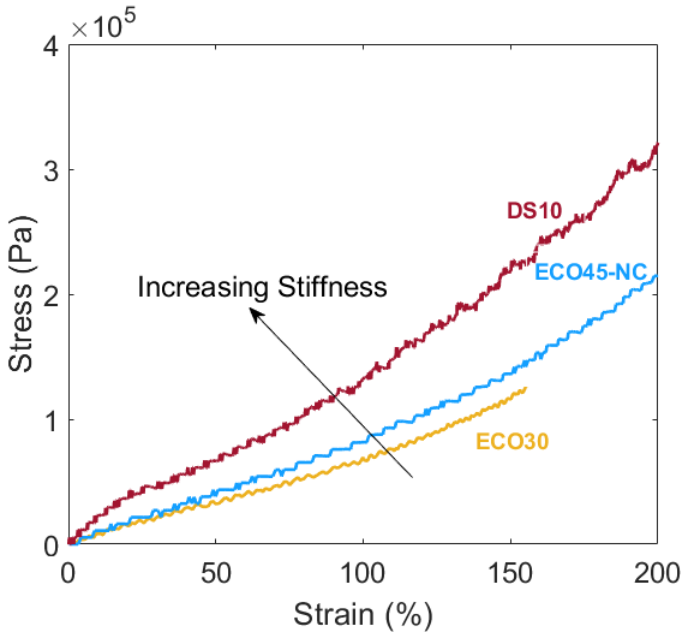

Figure 4.2. Stress-strain curves for all materials using tensile coupon testing.

All materials showed primarily linear behavior at low strains followed by some strain-hardening effect at higher strain values. This is due to their hyperelastic properties requiring higher stresses to achieve greater vertical stretching of the material. It can also be seen that ECO30 has the lowest range of stress values and the most gradual rise in its stress-strain curve. ECO45-NC had a slightly greater slope, while DS10 showed the steepest stress-strain curve

indicating that it is the stiffest material among the 3 testing silicones. The linear region between 0-100% strain was investigated to evaluate the Young's moduli in these materials using Hooke's Law from Equation 4.2.

$$\sigma = E\varepsilon \tag{4.2}$$

Here, σ is the stress, E is the Young's modulus, and ε is the strain given by the experimental data. The slopes from the stress-strain curves representing E, were calculated and recorded in Table 4.1. As noted earlier, DS10 had the highest Young's modulus value of 0.18 MPa, followed by ECO45-NC with 0.081 MPa, and finally, ECO30 with 0.068 MPa. It is also important to note that these materials show values at the lower range of documented values for human corneal Young's modulus [69]. These 3 materials can thus be used in the artificial cornea models to study behavior similar to human corneas that show similar stiffness.

Table 4.1. Young's Modulus values (in MPa) from tensile coupon testing results.

Human Cornea [69]	ECO30	ECO45-NC	DS10
0.05 - 0.40	0.0683 ± 0.0015	0.0812 ± 0.002	0.181 ± 0.004

4.2 Corneal Inflation Tests

4.2.1 Experimental Setup

Silicone models of the artificial cornea were obtained after the fabrication process described in Chapter 3. They were then clamped in the artificial anterior chamber and manometer setup before the channel was filled with water up to the "zero" pressure level. The goal of this experiment was to study the corneal behavior and stress-strain characteristics of these models under trephine inflation tests. Results can also be used to compare the cornea's apical rise in response to pressure increase, which has been previously studied in excised porcine and human

corneas [66]. To obtain data beyond 40 mmHg, the cornea test stand was moved from a desktop level to a lower height which allowed a maximum IOP of 120 mmHg to be simulated in the manometer column.

To record the inflation of the corneal button samples, a camera was placed for a direct side-view of the setup to record the corneal curvature throughout the experiment. The tests started at 0 mmHg, and the pressure was increased in the manometer by 5 mmHg increments each time. The camera was used to capture pictures of the corneal shape at each of these pressures and repeated until 120 mmHg. A clear background was also carefully placed so that a post-processing algorithm can be used to distinguish the cornea from the environment. A sample of the "original" pictures taken by this method is shown in the leftmost panel of Figure 4.3.

4.2.2 MATLAB Post-Processing

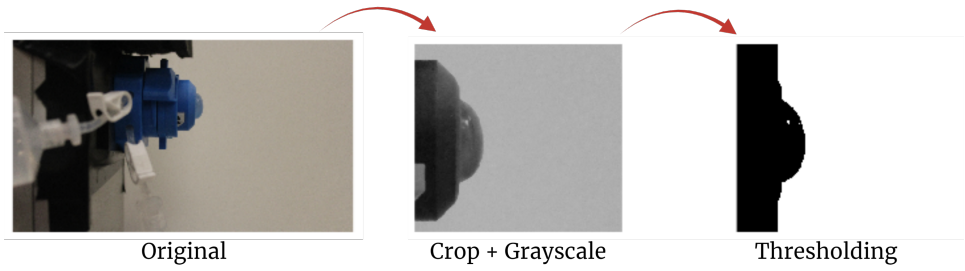

Figure 4.3. Inflation testing image processing procedure in MATLAB.

Similar to the tensile tests in the previous subchapter, it is essential to post-process the gathered images in order to obtain the corneas' apical rise and stress-strain data. Since the cornea samples were not speckled like the coupons tested earlier, a different MATLAB algorithm was developed for this purpose. The camera images are first loaded into the MATLAB script and converted to grayscale. This makes it easier to binarize the images by using a thresholding technique that enables us to separate the corneal shape from the background of the image. This process is outlined in Figure 4.3. An algorithm was then used on the first image (0 mmHg) to detect the apex of the cornea in terms of pixels, which was set as the initial corneal height. This

was repeated for the remaining images, and the pixel difference between the current frame and the initial image was calculated. These values were then scaled using real-world measurements of the anterior chamber's side profile to convert apical rise from pixels to millimeters. These apical rise curves were then plotted against the simulated intraocular pressure in the manometer channel and compared to corneal behavior in porcine and human samples.

4.2.3 Stress-Strain Calculations

The displacement results of the cornea can also be used to calculate their stress-strain curves that some studies have explored using thin membrane shell theory [64, 74]. The cornea hemispheres can be modeled as a shell with hydrostatic pressure on the interior surface (Fig. 4.4).

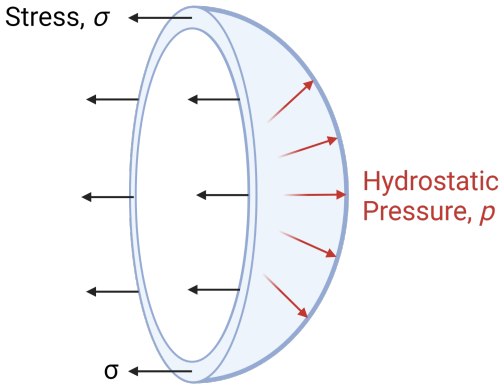

Figure 4.4. Cornea modeled as a thin membrane shell [5].

The stress (σ) for a particle element on the outer surface of the cornea can be derived (4.4) from the force balance in Equation 4.3. This is also known as a simplified Laplace's Law for corneoscleral biomechanics linking stress (σ), pressure (p), corneal radius of curvature (r), and central corneal thickness (t).

$$2\pi rt\sigma = \pi r^2 p \tag{4.3}$$

$$\sigma = \frac{pr}{2t} \tag{4.4}$$

Due to symmetry, it is assumed that the radial stress component as well as bending stresses on the corneal outer surface is zero [64]. Also, since the central thickness is small compared to the radius of curvature ($r/t < 0.1$), the cornea can be simplified as a thin membrane under plane stress conditions. The strain (ε) is thus given by the generalized Hooke's Law as follows:

$$\varepsilon = \frac{1}{E}(\sigma - \nu\sigma) = \frac{pr}{2Et}(1-\nu) \tag{4.5}$$

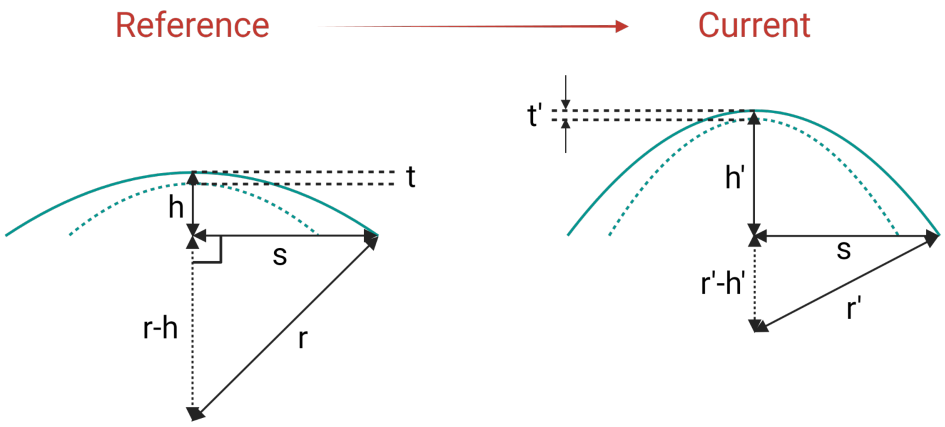

Figure 4.5. Reference and Current configurations (with exaggerated displacement) showing the change in corneal dimensions with increased pressure [5].

The Poisson's ratio, ν, is taken as 0.5 since the silicone materials are assumed to be incompressible solids. The apical rise (Δr), can thus be derived as:

$$\Delta r = \frac{pr^2}{2Et}(1-\nu) \tag{4.6}$$

This relationship can be rearranged to obtain E as a function of the apical rise as well. However, it must also be noted that the thickness as well as the radius of the cornea changes with increasing intraocular pressure. This can be closely observed in the reference and current configurations shown in Figure 4.5. Here, with a change in the corneal height (h), the radius (r), and thickness (t) must be calculated at each pressure increment. To account for this, we can use

the incompressibility assumption and derive the "current" thickness value (t') as follows:

$$t' = \frac{rht}{r'h'} \tag{4.7}$$

It can also be observed that the updated thickness values change depending on the current radius of curvature (r') and corneal height (h') values. These can also be calculated by a Pythagorean calculation involving the base radius (s) as given in equation 4.8.

$$r' = \frac{s^2 + h'^2}{2h'} \tag{4.8}$$

The base radius is assumed to stay constant in our setup of a clamped cornea. The corneal heights can be obtained from the apical rise measurements in MATLAB. With these mathematical relationships defined, the apical rise measurements can be used to solve for Young's moduli values (E). These can then be used to solve for strain values in the cornea (ε), and eventually the stress values (σ) to obtain a stress-strain curve for the designed inflation tests.

4.2.4 Apical Rise Results

Corneal button samples for all three silicone materials underwent inflation testing in order to study their mechanical behavior. All samples of DS10 and ECO45-NC were able to reach 120 mmHg without rupturing. However, the three ECO30 samples experienced over-inflation and failed in the 45-60 mmHg region. The apical rise results are shown in Figure 4.6. It is clearly seen that DS10 has a linear curve all the way up to 120 mmHg, while ECO45-NC starts showing non-linearity around 55 mmHg. ECO30 on the other hand, only follows a linear curve up to 25 mmHg, after which it becomes highly nonlinear. It is also important to note that the slope of pressure to apical rise ratio is highest in DS10 and the lowest in ECO30. Referring to the tensile test results earlier, it can be inferred that a higher Young's modulus (DS10) results in lower apical displacement, while a much softer material (ECO30) might show high displacements at low pressures.

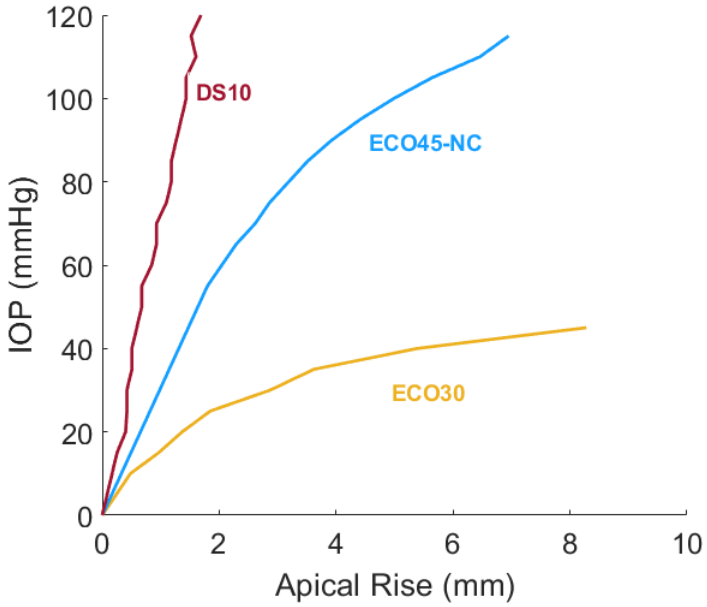

Figure 4.6. Apical rise for all materials at the tested intraocular pressures.

It is also essential that we compare these apical rise results to similar studies conducted in existing literature. Porcine and human corneal tissues have been used for trephine inflation tests and show results closest to the DS10 inflation results seen here [64, 65, 66]. Figure 4.7 shows all trials of DS10 overlaid with the line of best fit along with the documented human corneal behavior. It can be seen that the DS10 data points lie closely with the human cornea in the overlapping linear region up to 40 mmHg. After this, the collagenous fiber reorientation in actual corneal tissue causes a strain-hardening effect resulting in a non-linear increase in pressure for a relatively small apical rise. However, the corneal models use heterogeneous silicone material that does not exhibit such strain-hardening characteristics, and can only be used to capture this primary linear region. Regardless, it is of great significance that DS10 is able to show close correlation with human cornea in this pressure range. As seen in Figure 4.6, the slopes of ECO45-NC and ECO30 are even lower than DS10, and so are farther away from the expected human corneal behavior. This indicates that the DS10 model may be used for performance testing of commercial as well as the 3-in-1 device tonometer within the range of 0-40 mmHg. ECO45-NC also shows linear behavior up to 55 mmHg, and thus might be useful

in showing test results seen in a human cornea with slightly lower stiffness. ECO30 however, might lead to some inaccuracies above 25 mmHg simulated IOP, since it starts showing unstable displacements above this pressure level.

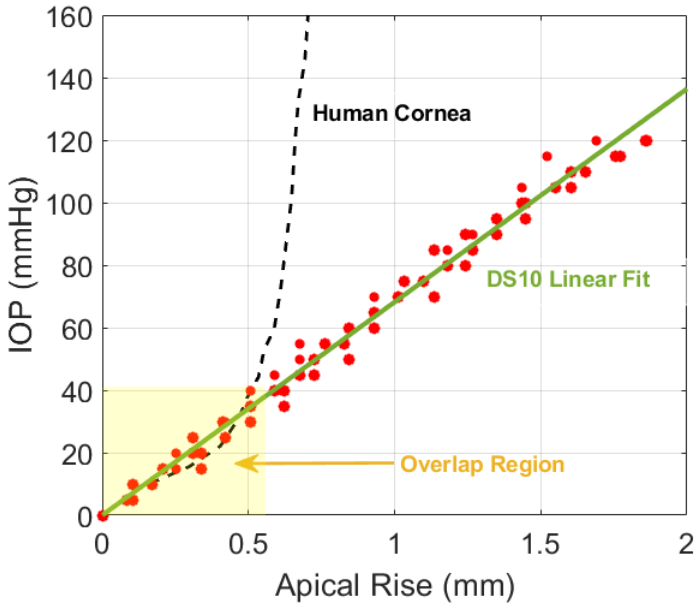

Figure 4.7. Inflation test results compared between DS10 and human cornea [64, 65, 66].

4.2.5 Stress-Strain Curves

As mentioned before, these apical rise results can be used to calculate values for Young's modulus in all the materials tested. After calculating the change in central thickness and radius of curvature, the corneal Young's moduli were recorded and listed in Table 4.2.

Table 4.2. Young's Modulus values (in MPa) from trephine inflation testing.

ECO30	ECO45-NC	DS10
0.054 ± 0.021	0.125 ± 0.012	0.236 ± 0.014

These tests confirm that DS10 was the material with the highest Young's modulus, followed by ECO45-NC, and lastly ECO30. Compared to the tensile test results earlier, the values obtained here are slightly greater than the ones in tensile coupon testing. This is due to the

great difference in geometry and testing standard of a tensile coupon versus the cornea model. The DS10 values in the inflation test result in a Young's modulus that falls within the 0.20-0.30 corneal stiffness range observed in vivo at a healthy IOP level (around 15 mmHg) [68]. So, inflation results might show a greater level of accuracy than coupon tensile testing in determining the stiffness acquired using this artificial cornea model's geometry.

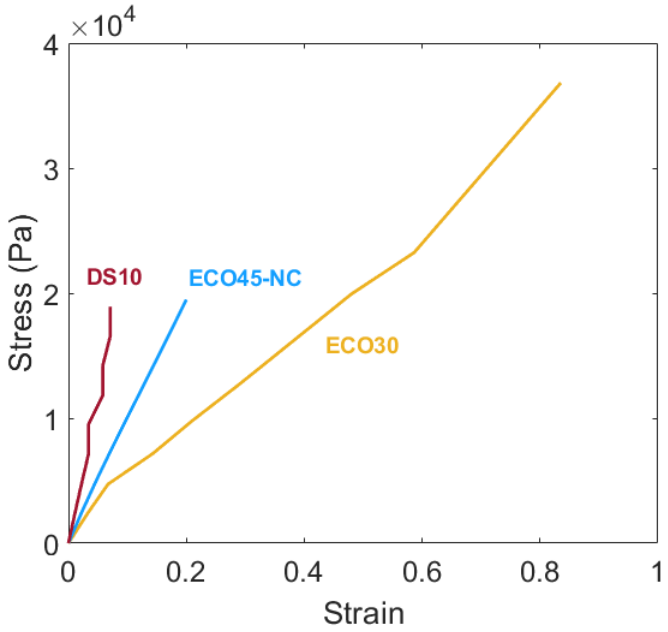

Figure 4.8. Stress-strain results obtained from inflation testing on all silicone materials.

Stress-strain curves were also obtained from the inflation test results as specified (Fig. 4.8. It was observed that the three materials follow very similar trends from tensile testing. DS10 being the stiffest, showed the steepest slope followed by ECO45-NC and ECO30. DS10 and ECO45-NC continue to show largely linear curves while ECO30 does not. It also shows an extremely large amount of strain at the same pressures compared to the other two materials. This is due to the large corneal displacement observed earlier in the apical rise plot, leading to a large amount of strain.

Chapter 4, in part, has been accepted for publication of the material as it may appear in Information Storage and Processing Systems, 2023. Laha, Avinash; Srinath, Aravind; Talke, Frank E., ASME, 2023. The thesis author was a researcher and co-author of this paper.

Chapter 5

Performance Testing

5.1 Testing with a Commercial Tonometer

5.1.1 Testing Methods

For performance testing of the artificial cornea system, a commercially available iCare TonoVet Plus tonometer was acquired. This uses the rebound tonometry technique and measures the outgoing and incoming speeds of a miniature probe that is allowed to rebound off the corneal surface. The rebound speed can then be used to determine the intraocular pressure in the eye since a greater IOP results in greater relative ocular rigidity and thus, a higher rebound speed. These readings are fairly quick, and easy to use without specialized medical training, and was thus a valid choice for testing in the laboratory environment. The tonometer then repeats this process for a total of 6 times in order to obtain an average final measurement of IOP.

To test this device with the artificial cornea, the setup was moved to the desktop stand such that the manometer column height allowed for an IOP range of 0 to 40 mmHg. Since this device is usually calibrated for veterinary purposes, the tests were conducted on the "lapine" setting since existing studies have indicated geometrical similarities between human and rabbit cornea [75]. The tonometer was then held upright with the probe pointing at the apex of the cornea. A neoprene pad was also mounted above the anterior chamber to allow a stable resting area for the tonometer's forehead support. An image of this setup is shown in Figure 5.1. The readings started with IOP = 0 mmHg, and 6 readings were taken at pressure increments of

5 mmHg. This process was then repeated with all fabricated corneas to compare readings at different corneal stiffnesses.

Figure 5.1. Setup for testing with the commercial tonometer (TonoVet Plus).

5.1.2 Experimental Results

The readings for all the corneal samples were compiled and plotted in MATLAB as shown in Figure 5.2. All three chosen materials exhibited a linear increase with an increase in manometer pressure. This is in accordance with the physical expectation that a higher internal pressure results in a greater rebound speed, and therefore a higher tonometer reading. The three materials also had very similar slopes as well - 0.307 (ECO30), 3.313 (ECO45-NC), and 0.287 (DS10). However, these three curves did not overlap upon each other, but instead show different y-intercepts indicating a dependence on the specific stiffness of the cornea. ECO30 had the lowest range of tonometer readings ranging from 14 to 27 mmHg. ECO45-NC had a slightly higher range between 18 and 31 mmHg, while DS10 showed the highest range of values between 26 and 39 mmHg. Since DS10 has the highest Young's modulus, it contributes to a higher rebound force and the highest range of values as well. ECO30 having the lowest Young's modulus, thus shows the lowest range of tonometer readings.

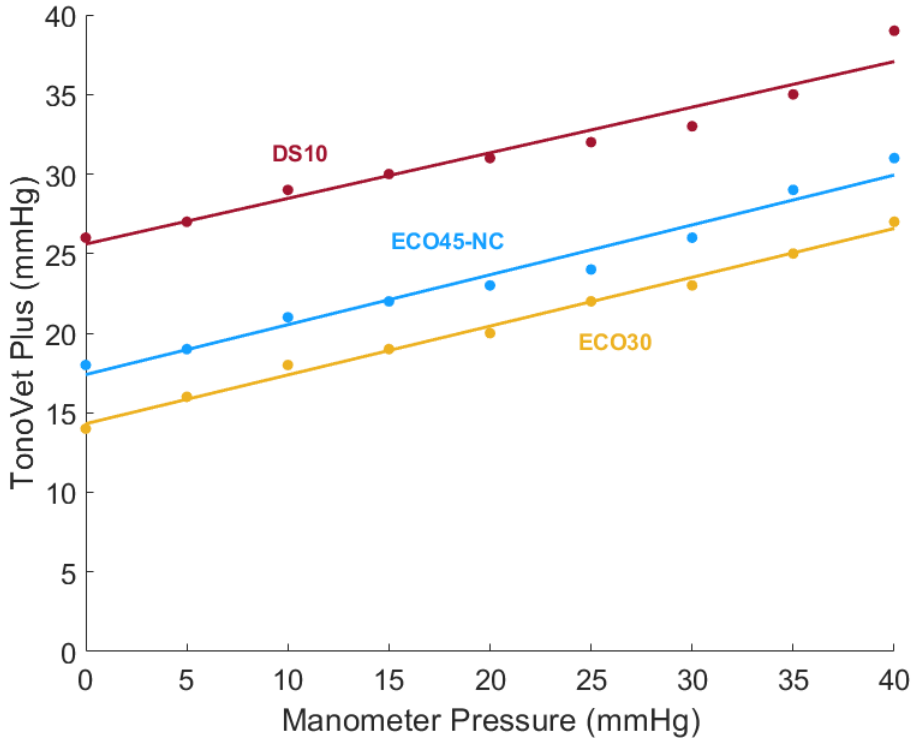

Figure 5.2. Averaged TonoVet Plus readings obtained for increasing manometer pressure values.

Although the tests conducted with the TonoVet Plus tonometer confirm a steady linear increase with IOP, none of the samples showed a 1:1 ratio between tonometer readings and pressure. Ideally, the manometer pressure change should match closely with the tonometer readings. This discrepancy could potentially be due to the fact that the device is only calibrated for animal corneas, but the mechanical and geometrical properties of a human cornea varies in different ways. It could also be due to the tonometer's measurement error, as various studies indicate a very narrow range beside which the device provides inaccurate results, especially at low or very high IOP levels [76, 77]. However, another source of error could also be attributed to the cornea design itself, and so, the model must be tested against more accurate tonometers, ideally designed for human corneas in future studies. Regardless, the model shows valid initial proof-of-concept with the expected linear dependency on increasing IOP.

5.2 Testing with the 3-in-1 Device

5.2.1 Tonometer Procedure

For testing the newly developed non-contact tonometer system inside the 3-in-1 handheld device, the device was placed on a platform with the tonometer's eye hole facing the mounted cornea. The phantom eye setup remained the same as before, with the IOP range being tested falling between 0 and 40 mmHg. The touchscreen of the device can be used to select the appropriate mode in the main menu, after which the tonometer test automatically initiates. After a 2-second pause, the LED light ring placed behind the Placido cone turns on to project the rings onto the cornea sample. The uploaded program then generates 3 separate air puffs by switching the channels of the solenoid valve that controls the air flow from the air regulator. These puffs also have an additional 2-second interval in between them to properly ensure the cornea returns back to an undeformed state before obtaining a successive reading. The air regulator is set to generate these puffs at 5 psi (260 mmHg) while the camera placed in-line with this setup records a video at 120 FPS to record corneal deformation. Since the length of these puffs are around 100 milliseconds, this frame rate results in 12 consecutive frames that clearly show a fully deformed Placido ring configuration in response to each puff. Keeping the air puff pressure constant, the difference in Placido ring deformation at varying IOP levels can be further analyzed to calibrate these readings.

5.2.2 MATLAB Analysis

A MATLAB script was developed to analyze the Placido ring deformation observed in the tonometer videos. To analyze the deformation of the cornea during applanation, several noise filtering and image detection algorithms were implemented with the goal of recording the centroid displacement of the Placido ring cluster at the different IOP levels. The videos were first sliced into individual frames and imported into MATLAB. The frames were then cropped to isolate the two projected rings on the corneal surface. The videos recorded by the

camera were in grayscale, and did not require an added thresholding algorithm as used during the post-processing technique for corneal inflation testing earlier. However, a low-pass digital filter (wiener2) was used to remove noise signals observed outside of the Placido ring cluster in the processed images. This method uses a pixel-wise adaptive algorithm and a statistics-based comparison to effectively minimize the signal-to-noise ratio [78]. Next, an image contouring method (activecontour) used a mask area defined to be only around the ring cluster to detect this contour after segmentation over a 100 iterations. This allows the rings to be completely isolated from background noise through this clustering algorithm.

Lastly, a built-in MATLAB function for image detection (regionprops) was utilized to detect the centroid of this ring cluster and tracked over each single frame of the video. The x- and y-coordinates of these detected centroid points were then used to calculate the difference in centroid location using the distance formula in equation 5.1. Here, x and y represent the centroid coordinates in the current frame, and x_i and y_i are the initial coordinates observed in the first frame of the test. The resulting $d_{centroid}$ measures the total displacement of the Placido ring centroid through the entire test.

$$d_{centroid} = \sqrt{(x - x_i)^2 + (y - y_i)^2} \tag{5.1}$$

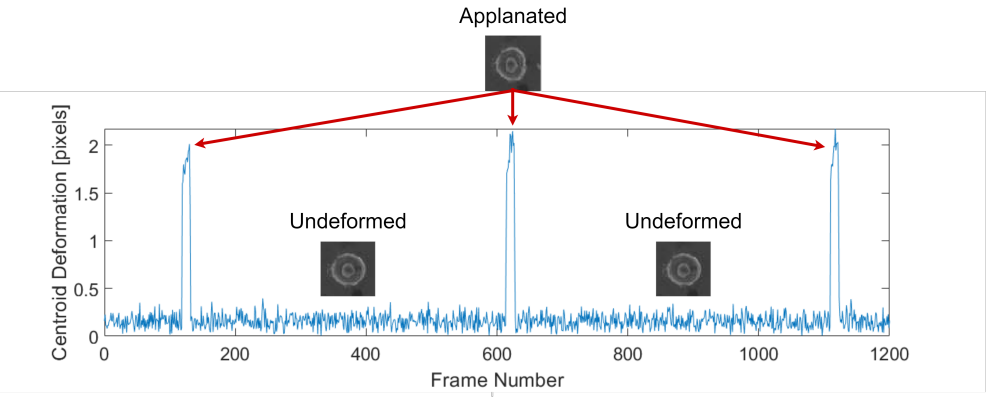

Figure 5.3. Centroid displacement spikes detected by the MATLAB script. An example frame of an undeformed as well as applanated Placido ring configuration is overlaid for clarity.

An example of the resulting plot is shown in Figure 5.3 that indicates centroid movement in pixels over all the frames in the video. It can be seen that there is little to no movement of the centroid before the puff is initiated. When the air puff hits the cornea, a visible spike can be observed which corresponds to the displaced Placido rings upon applanation. The centroid remains at this location for around 100 milliseconds (duration of the air puff) before returning to its original position. This repeats for the other 2 generated puffs as well, after which an aggregate value can be taken among the three spikes to obtain a final reading of the centroid displacement. As seen in this example figure, the three puffs yield consistent centroid displacement values (maximum variation of ± 0.1 pixels), indicating a highly repeatable tonometer measurement principle. This displacement is then converted to millimeters by scaling the pixels to real-world measurements. This entire process was finally repeated with all cornea samples at pressure levels up to 40 mmHg, and compared to observe the corneal response to different levels of intraocular pressure.

5.2.3 Placido Ring Displacement Results

The Placido ring centroid displacement values for all corneal materials were plotted on Figure 5.4. All the samples exhibited an inverse linear relationship with increasing pressure in the manometer channel. A higher IOP contributes to a greater internal resistive force during the tonometer applanation. Thus, this results in a much lower deformation of the cornea, and therefore a lower Placido ring displacement as well. All three materials also showed a high correlation coefficient ($R^2 > 0.97$) indicating a strong linear relationship between corneal deformation and pressure. It can however be seen that ECO30 has a much steeper downwards slope (-9 μm/mmHg) when compared to ECO45-NC (-4.6 μm/mmHg) and DS10 (-4.2 μm/mmHg). It also shows a much greater range of Placido ring displacement values when compared to the other two. In fact, the range of Placido ring displacement seems to also be negatively correlated with an increasing stiffness in the material. Since DS10 has the highest Young's modulus value, the added stiffness results in a much lower corneal deformation at the tested pressure values.

Consequently, ECO30 shows the greatest ring displacement due to a lower Young's modulus value, and ECO45-NC falls in between these two materials for its intermediate stiffness. This implies that a lower Young's modulus thus contributes to lower resistive corneal forces upon air puff applanation and shows greater Placido ring displacement within the tested pressure range.

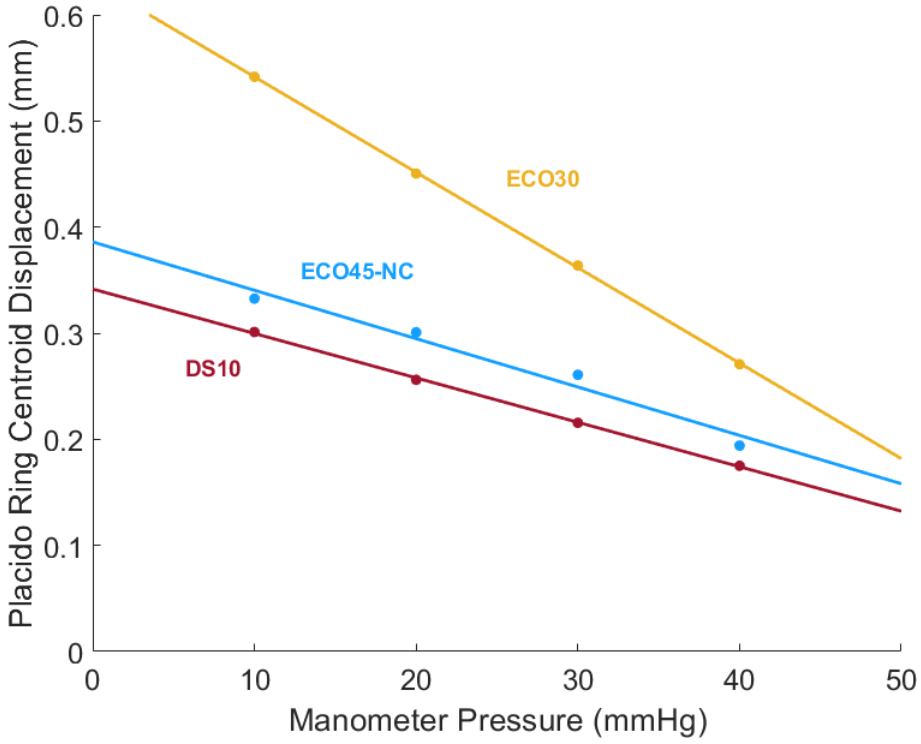

Figure 5.4. Centroid displacement of Placido ring projections obtained for all materials at increasing manometer pressures.

Since DS10 was determined to be closest to human corneal behavior in this study, closer analysis of these samples can reveal a calibration curve useful for calculation of the IOP readings from this 3-in-1 tonometer system. Table 5.1 lists the range of Placido ring displacements observed at each of the tested pressure values. For a "normal" range of eye pressure in a healthy eye (10-21 mmHg), the Placido ring centroid may be expected to displace between the values of 0.30 mm and 0.26 mm, respectively. A high IOP (at risk for glaucoma) may then be associated with a Placido ring displacement of 0.22 mm or below as observed in the range above 30 mmHg. A lower eye pressure on the other hand may be observed through a Placido ring displacement

greater than 0.30 mm. It is also important to note that ECO45-NC still falls close to the lower end of human corneal ranges, and might provide a helpful calibration curve for a human eye of lower ocular rigidity.

Table 5.1. The 3-in-1 device's tonometer calibration table based on DS10 centroid displacement values.

Intraocular Pressure (mmHg)	0	10	20	30	40
Placido Ring Centroid Displacement (mm)	0.34	0.30	0.26	0.22	0.17

Both ECO45-NC and DS10 also showed linear behavior during inflation testing in the range 0-40 mmHg, which is similar to the linear behavior seen at lower strains in human corneas. This may also correlate to a reduced error in terms of capturing actual corneal behavior at these pressures. However, it is important to follow up the findings from these experiments with similar inflation and tonometer testing on excised human corneas to compare centroid displacement in the Placido ring projections in healthy and glaucomatous eyes. Yet, these measurements still give promising preclinical data that validates the working principle of this tonometer. Values similar to DS10 and ECO45-NC centroid displacements may be expected when testing this novel instrument on a human eye, which can further solidify future calibration and validation of similar handheld instruments.

Chapter 5, in part, has been accepted for publication of the material as it may appear in Information Storage and Processing Systems, 2023. Laha, Avinash; Srinath, Aravind; Talke, Frank E., ASME, 2023. The thesis author was a researcher and co-author of this paper.

Chapter 6

Summary and Future Work

6.1 Summary

Glaucoma is an eye disease that is the leading cause of irreversible blindness in the world currently. Although familial history, aging, and general physical health can put a patient at risk for glaucoma, it is often associated with an elevated intraocular pressure (IOP) causing damage to retinal ganglion cells and the optic nerve. Since therapeutic and surgical cures can be difficult to acquire at extreme stages, regular monitoring of IOP must be performed. Thus, easy-to-use self-examining ophthalmic devices are highly desirable to reduce the inconvenience of repeated visits to eye clinics in person.

Existing tonometer devices cannot easily be used without a medically trained professional present. Some handheld tonometers have entered the market space recently that allow efficient testing of eye pressures, but still show levels of inaccuracy at high IOP. Although several other handheld devices have attempted in achieving individual ophthalmic tests for glaucoma, a comprehensive device with multiple examinations does not currently exist in the commercial market. The Talke Biomedical Device Laboratory has attempted to address this existing gap with a novel 3-in-1 handheld device that combines three common glaucoma-screening instruments - namely, a slit lamp biomicroscope, visual acuity screener, and non-contact tonometer. This allows patients to conveniently performing multiple ocular exams without the need for a physician, and also have the option of sharing these results with a doctor via the internet if further analysis

is required. A minimum viable product has been achieved using 3D printing and other rapid prototyping techniques.

To progress the validation and performance metrics of this device, an artificial cornea model was investigated with the goal of obtaining pre-clinical IOP readings using the tonometer system. This thesis focused on the material selection and characterization of various silicone materials for the fabrication of these models. A geometrical design of the desired cornea samples imitating the dimensions of human corneas was discussed in detail. An artificial anterior chamber and manometer system was also designed to develop a ”phantom eye” setup that is capable of simulating a range of intraocular pressures, including elevated values at risk for glaucoma.

The silicone materials were further studied through uniaxial tensile tests to obtain Young's modulus values in the initial linear region (0-100% strain). Inflation tests were also performed on all chosen silicone materials to compare corneal behavior with documented studies on trephine human corneal samples. DragonSkin 10 (DS10) was shown to be the silicone material closest to average documented Young's modulus values in in-vivo human corneas. It also showed closest agreement with actual corneal tissue under inflation testing within the range of 0-40 mmHg. Since the current phase of cornea modeling considers a homogeneous silicone material, DS10 only captures the initial linear apical rise at lower strains and is unable to match the strain-stiffening observed in collagen reorientation in human cornea. However, this material showed promise in allowing preliminary calibration data to be collected at this pressure range with the newly developed handheld tonometer.

The designed phantom eye apparatus was tested at IOP ranges between 0 and 40 mmHg using both a commercial tonometer as well as the non-contact tonometer of the handheld 3-in-1 device. All three silicone materials were tested with a rebound tonometer, which was successful in capturing a linear increase in IOP readings as manometer pressure was increased. The readings also showed a direct correlation with the stiffness of each cornea material. However, this method of pressure measurement needs to be confirmed using more accurate tonometers specifically designed for human use in the future. The 3-in-1 device's tonometer showed an inverse linear

relationship between Placido ring deformation and increasing IOP in the manometer channel. This was attributed to higher corneal resistance causing lower Placido ring displacement at higher pressures. These readings also showed a similar correlation with varying corneal stiffnesses similar to the rebound tonometer results. The values for Placido ring displacement observed for DS10 were closely documented for future reference in calibration of this device.

6.2 Future Work

This phase of research and performance testing was successful in achieving a proof-of-concept for a tunable geometrical and mechanical model imitating a human cornea. However, it is imperative to expand these findings to a better material model that is capable of capturing the anisotropic hyperelasticity exhibited by human corneas at large strains. Silicone-based composite materials may provide such a strain-hardening behavior that can potentially improve the behavior of these models. Furthermore, the optical properties of these samples may be improved by exploring other surface-treatment methods following the success of polished 3D-printed molds presented in this work. Additionally, this cornea model may also be extended to design a complete ocular globe model with physical boundary conditions that more closely relate to in-vivo conditions.

The results from the tensile testing as well as inflation testing of the cornea samples can be used to develop a numerical finite element model that accurately captures the mechanical behavior of the cornea. The stress-strain relationships can be studied using hyperelastic material models such as Mooney-Rivlin or Gent models, and can be curve-fitted to obtain the material coefficients that define these equations. An accurate numerical model can then be analyzed under different boundary and loading conditions to study the corneal response to inflation and air puff applanation as observed in this work, as well as other tonometry methods.

Additionally, the tonometer results obtained by these cornea materials (especially DS10) can be seen as promising pre-clinical calibration data for a newly developed handheld tonometer

device. These readings can be further confirmed by comparing IOP readings with the 3-in-1 device on excised porcine or human corneas in the future. The cornea models are also planned for intermediate validation using a commercially-available Goldmann Applanation tonometer, owing to its high clinical success in in-vivo IOP measurements. These studies can further solidify the similarities and limits of the artificial cornea models with human tissue.

Future work for various improvements on the 3-in-1 device itself is also planned to build upon its current efficiency and convenience in self-examination of the eye. To decrease some of the bulky components of the device, a modular housing is being developed with interchangeable components for all three current instruments. This would allow the user to exchange different instruments according to their needs, and also reduce the weight of the current 3-in-1 device. New methods of tonometer applanation detection are also being explored involving angled infrared sensing that would allow placement of the air puff nozzle for a perpendicular corneal applanation force similar to existing devices. Moreover, expansion of the visual acuity screener to include letters other than the 'E' optotype can also improve this test procedure. The slit lamp system can also be expanded to a stereo camera setup to obtain a 3-dimensional image of the anterior chamber for a more realistic view into the patient's eye.

Most importantly, the success of these artificial corneas paves the way for the clinical testing phase of the device. Tests with excised human corneas and eye globes can further help improve the understanding of corneal response to glaucomatous IOP levels. Eventual patient usage and feedback of the device will enhance the impact of this work to improve the prospect of ophthalmic self-examination in the future.

References

[1] Li Guo, Stephen E. Moss, Robert A. Alexander, Robin R. Ali, Frederick W. Fitzke, and M. Francesca Cordeiro. Retinal Ganglion Cell Apoptosis in Glaucoma Is Related to Intraocular Pressure and IOP-Induced Effects on Extracellular Matrix. *Investigative Ophthalmology Visual Science*, 46(1):175–182, 01 2005.

[2] R.N. Weinreb, J.D. Brandt, D. Garway-Heath, and F. Medeiros. *Intraocular Pressure*. Consensus series. Kugler Publications, 2007.

[3] Robert J Casson, Glyn Chidlow, John PM Wood, Jonathan G Crowston, and Ivan Goldberg. Definition of glaucoma: clinical and experimental concepts. *Clinical & Experimental Ophthalmology*, 40(4):341–349, 2012.

[4] John C. Morrison, Elaine C. Johnson, William Cepurna, and Lijun Jia. Understanding mechanisms of pressure-induced optic nerve damage. *Progress in Retinal Research*, 24(2):217–240, March 2005. Funding Information: Work supported in part by National Institutes of Health Grant R01-10145 (NEI) and unrestricted funds from Research to Prevent Blindness. Dr. Morrison is a 2001 Lew Wasserman RPB Scholar.

[5] Figure partially created with BioRender.com.

[6] David Crabb. A view on glaucoma - are we seeing it clearly? *Eye (London, England)*, 30, 11 2015.

[7] Ronnie George, Smita Panda, and Lingam Vijaya. Blindness in glaucoma: primary open-angle glaucoma versus primary angle-closure glaucoma—a meta-analysis. *Eye*, 36:1–7, 10 2021.

[8] Karen Allison, Deepkumar Patel, and Omobolanle Alabi. Epidemiology of glaucoma: The past, present, and predictions for the future. *Cureus*, 12, 11 2020.

[9] Robert Feder, Timothy Olsen, Bruce Prum, C. Summers, Randall Olson, Ruth Williams, and David Musch. Comprehensive adult medical eye evaluation preferred practice pattern® guidelines. *Ophthalmology*, 123, 11 2015.

[10] Thomas Ravi, Klaus Loibl, and Rajul Parikh. Evaluation of a glaucoma patient. *Indian journal of ophthalmology*, 59 Suppl:S43–52, 12 2011.

[11] M. Bach. Electrophysiological approaches for early detection of glaucoma. *European Journal of Ophthalmology*, 11(2_suppl):41–49, 2001.

[12] David Musch, Brenda Gillespie, Leslie Niziol, Paul Lichter, and Rohit Varma. Intraocular pressure control and long-term visual field loss in the collaborative initial glaucoma treatment study. *Ophthalmology*, 118:1766–73, 05 2011.

[13] Elliot Kirstein, Ahmed Elsheikh, and Pinakin Gunvant. *Tonometry - Past, Present and Future*. 11 2011.

[14] Paolo Brusini, Maria Letizia Salvetat, and Marco Zeppieri. How to measure intraocular pressure: An updated review of various tonometers. *Journal of Clinical Medicine*, 10, 2021.

[15] HAAG-STREIT USA. At 900 goldmann applanation tonometer, 2023. Last accessed 22 May, 2023.

[16] HAAG-STREIT USA. Perkins mk3, 2023. Last accessed 22 May, 2023.

[17] Reichert Ametek. Tono-pen avia, 2023. Last accessed 22 May, 2023.

[18] John Gloster and Edward S. Perkins. The validity of the imbert-flick law as applied to applanation tonometry. *Experimental eye research*, 2:274–83, 1963.

[19] Marco Zeppieri and Bharat Gurnani. Applanation tonometry. In *StatPearls [Internet]*. StatPearls Publishing, 2022.

[20] Keeler. Pulsair desktop tonometer, 2023. Last accessed 22 May, 2023.

[21] iCare. icare ic100, 2023. Last accessed 22 May, 2023.

[22] MJ Moseley, NM Evans, and AR Fielder. Comparison of a new non-contact tonometer with goldmann applanation. *Eye*, 3(3):332–337, 1989.

[23] Branislav Hučko, Ľuboš Kučera, Stanislav Ďuriš, Peter Pavlásek, Jan Rybář, and Juraj Hodál. Modeling of cornea applanation when measuring eye pressure. In *Current Methods of Construction Design: Proceedings of the ICMD 2018*, pages 287–294. Springer, 2020.

[24] M Bruce Shields. The non-contact tonometer. its value and limitations. *Survey of ophthalmology*, 24(4):211–219, 1980.

[25] Feng Gao, Xu Liu, Qing Zhao, and Yingzhe Pan. Comparison of the icare rebound tonometer and the goldmann applanation tonometer. *Experimental and Therapeutic Medicine*, 13(5):1912–1916, 2017.

[26] Behrooz Kouchaki, Hassan Hashemi, Abbasali Yekta, and Mehdi khabazkhoob. Comparison of current tonometry techniques in measurement of intraocular pressure. *Journal of current ophthalmology*, 29(2):92–97, 2017.

[27] Jessica Massie, Sandra S Block, and Priya Morjaria. The role of optometry in the delivery of eye care via telehealth: A systematic literature review. *Telemedicine and e-Health*, 28(12):1753–1763, 2022.

[28] Keeler. Tonocare, 2023. Last accessed 22 May, 2023.

[29] iCare. icare home, 2023. Last accessed 22 May, 2023.

[30] Steve Y-W Liang, Graham A Lee, and David Shields. Self-tonometry in glaucoma management—past, present and future. *Survey of ophthalmology*, 54(4):450–462, 2009.

[31] Monica K Ertel, Leonard K Seibold, Jennifer L Patnaik, and Malik Y Kahook. Comparison of intraocular pressure readings with perkins, tonopen, icare 200, and icare home to manometry in cadaveric eyes. *International Journal of Ophthalmology*, 15(12), 2022.

[32] PL Atkinson, PK Wishart, JN James, SA Vernon, and F Reid. Deterioration in the accuracy of the pulsair non-contact tonometer with use: need for regular calibration. *Eye*, 6(5):530–534, 1992.

[33] Leon W Herndon. Measuring intraocular pressure-adjustments for corneal thickness and new technologies. *Current opinion in ophthalmology*, 17(2):115–119, 2006.

[34] Ashkan Eliasy, Kai-Jung Chen, Riccardo Vinciguerra, Osama Maklad, Paolo Vinciguerra, Renato Ambrósio Jr, Cynthia J Roberts, and Ahmed Elsheikh. Ex-vivo experimental validation of biomechanically-corrected intraocular pressure measurements on human eyes using the corvis st. *Experimental eye research*, 175:98–102, 2018.

[35] Peter Pavlásek, Jan Rybář, Stanislav Ďuriš, Branislav Hučko, Miroslav Chytil, Alena Furdová, Sylvia Lea Ferková, Juraj Sekáč, Vítězslav Suchỳ, and Patrik Grosinger. Developments and progress in non-contact eye tonometer calibration. *Measurement Science Review*, 20(4):171–177, 2020.

[36] Michael J Doughty and Mohammed L Zaman. Human corneal thickness and its impact on intraocular pressure measures: a review and meta-analysis approach. *Survey of ophthalmology*, 44(5):367–408, 2000.

[37] Barbara K Pierscionek, M Asejczyk-Widlicka, and Ronald A Schachar. The effect of changing intraocular pressure on the corneal and scleral curvatures in the fresh porcine eye. *British Journal of ophthalmology*, 91(6):801–803, 2007.

[38] Wenhan Yu, Guiqun CaO, Jinghua Qiu, Xuyang Liu, Jia Ma, Ni Li, Man Yu, Naihong Yan, Lei Chen, and Iok-Hou Pang. Evaluation of monkey intraocular pressure by rebound tonometer. *Molecular vision*, 15:2196, 2009.

[39] OE Babalola, AV Kehinde, AC Iloegbunam, T Akinbinu, C Moghalu, and I Onuoha. A comparison of the goldmann applanation and non-contact (keeler pulsair easyeye) tonometers and the effect of central corneal thickness in indigenous african eyes. *Ophthalmic and Physiological Optics*, 29(2):182–188, 2009.

[40] E Eriksson, L Davidsson, and R Brautaset. A comparative study of the tonometers: Goldmann applanation, perkins, tono-pen xl and reichert 7cr. *International Journal of Ophthalmic Practice*, 2(6):246–251, 2011.

[41] Shalini Mohan, Satyaprakash Tiwari, Arvind Jain, Jaya Gupta, and Surendra Kumar Sachan. Clinical comparison of pulsair non-contact tonometer and goldmann applanation tonometer in indian population. *Journal of Optometry*, 7(2):86–90, 2014.

[42] Hidenaga Kobashi and Masaaki Kobayashi. 3d-printed eye model: Simulation of intraocular pressure. *Plos one*, 18(3):e0282911, 2023.

[43] Jan Rybář, Miroslav Chytil, Stanislav Ďuriš, Branislav Hučko, Filip Maukš, and Peter Pavlásek. Use of suitable materials such as artificial cornea on eye model for calibration of optical tonometers. In *AIP Conference Proceedings*, volume 2029, page 020067. AIP Publishing LLC, 2018.

[44] Philip Schwinn. *Design and Rapid Prototyping of a Multifunctional Portable Device for Ophthalmic Examinations*. Technical University Munich School of Engineering and Design, Institute of Micro Technology and Medical Device Technology, Arcisstraße 21, 80333 München, Germany, 2022.

[45] Thomas Kuriakose and Thomas Kuriakose. The slit lamp examination. *Clinical Insights and Examination Techniques in Ophthalmology*, pages 55–62, 2020.

[46] Shenming Hu, Hong Wu, Xinze Luan, Zhuoshi Wang, Mary Adu, Xiaoting Wang, Chunhong Yan, Bo Li, Kewang Li, Ying Zou, Xiaoya Yu, Xiangdong He, and Wei He. Portable handheld slit-lamp based on a smartphone camera for cataract screening. *Journal of Ophthalmology*, 2020, 2020.

[47] Alex Phan, Buu Truong, Benjamin Suen, Gerrit Melles, and Frank E Talke. Portable ophthalmic device for remote slit-lamp examinations and visual acuity screening. In *Information Storage and Processing Systems*, volume 84799, page V001T07A002. American Society of Mechanical Engineers, 2021.

[48] Ai-Hong Chen, Fatin Nur Najwa Norazman, and Noor Halilah Buari. Comparison of visual acuity estimates using three different letter charts under two ambient room illuminations. *Indian journal of ophthalmology*, 60(2):101, 2012.

[49] Paulus TVM de Jong. A history of visual acuity testing and optotypes. *Eye*, pages 1–12, 2022.

[50] Lingge Suo, Xianghan Ke, Di Zhang, Xuejiao Qin, Xuhao Chen, Ying Hong, Wanwei Dai, Defu Wu, Chun Zhang, and Dongsong Zhang. Use of mobile apps for visual acuity assessment: Systematic review and meta-analysis. *JMIR mHealth and uHealth*, 10(2):e26275, 2022.

[51] Agnieszka Boszczyk, Henryk Kasprzak, and Joanna Przeździecka-Dołyk. Novel method of measuring corneal viscoelasticity using the corvis st tonometer. *Journal of Clinical Medicine*, 11(1):261, 2022.

[52] F Cavas-Martínez, E De la Cruz Sánchez, J Nieto Martínez, FJ Fernández Cañavate, and DG Fernández-Pacheco. Corneal topography in keratoconus: state of the art. *Eye and vision*, 3:1–12, 2016.

[53] Buu Kim Truong. *Design and Rapid Prototyping of Portable Ophthalmic Measurement Instruments for Frequent Self-monitoring of Eye Conditions*. University of California, San Diego, 2020.

[54] Dirk Schuster. *Development of a Handheld Funduscope and Data Analysis for a Portable Pneumatic Tonometer*. Technical University Munich School of Engineering and Design, Institute of Micro Technology and Medical Device Technology, Arcisstraße 21, 80333 München, Germany, 2021.

[55] Jie Zhu, Ellean Zhang, and Katia Rio-Tsonis. *Eye Anatomy*. 11 2012.

[56] Barry D Kels, Andrzej Grzybowski, and Jane M Grant-Kels. Human ocular anatomy. *Clinics in dermatology*, 33(2):140–146, 2015.

[57] F. Grehn and R. Stamper. *Glaucoma*. Essentials in Ophthalmology. Springer Berlin Heidelberg, 2009.

[58] Kalyan C Katuri, Sanjay Asrani, and Melur K Ramasubramanian. Intraocular pressure monitoring sensors. *IEEE Sensors Journal*, 8(1):12–19, 2008.

[59] Mittanamalli S Sridhar. Anatomy of cornea and ocular surface. *Indian journal of ophthalmology*, 66(2):190, 2018.

[60] Andrew Siu and Peter Herse. The effect of age on human corneal thickness: statistical implications of power analysis. *Acta ophthalmologica*, 71(1):51–56, 1993.

[61] Danilo A Jesus, Renata Kedzia, and D Robert Iskander. Precise measurement of scleral radius using anterior eye profilometry. *Contact Lens and Anterior Eye*, 40(1):47–52, 2017.

[62] Richard E Norman, John G Flanagan, Sophie MK Rausch, Ian A Sigal, Inka Tertinegg, Armin Eilaghi, Sharon Portnoy, John G Sled, and C Ross Ethier. Dimensions of the human sclera: thickness measurement and regional changes with axial length. *Experimental eye research*, 90(2):277–284, 2010.

[63] Luigina Sorbara, Jyotsna Maram, Desmond Fonn, Craig Woods, and Trefford Simpson. Metrics of the normal cornea: anterior segment imaging with the visante oct. *Clinical and experimental optometry*, 93(3):150–156, 2010.

[64] Kevin Anderson, Ahmed El-Sheikh, and Timothy Newson. Application of structural analysis to the mechanical behaviour of the cornea. *Journal of the Royal Society Interface*, 1(1):3–15, 2004.

[65] Ahmed Elsheikh and Defu Wang. Numerical modelling of corneal biomechanical behaviour. *Computer methods in biomechanics and biomedical engineering*, 10(2):85–95, 2007.

[66] Ahmed Elsheikh, Daad Alhasso, and Paolo Rama. Biomechanical properties of human and porcine corneas. *Experimental eye research*, 86(5):783–790, 2008.

[67] Girma J Orssengo and David C Pye. Determination of the true intraocular pressure and modulus of elasticity of the human cornea in vivo. *Bulletin of mathematical biology*, 61(3):551–572, 1999.

[68] Po-Jen Shih, Chun-Ju Huang, Tzu-Han Huang, Hung-Chou Lin, Jia-Yush Yen, I Wang, Hui-Jyun Cao, Wen-Pin Shih, and Chi-An Dai. Estimation of the corneal young's modulus in vivo based on a fluid-filled spherical-shell model with scheimpflug imaging. *Journal of ophthalmology*, 2017, 2017.

[69] Kirsten E Hamilton and David C Pye. Young's modulus in normal corneas and the effect on applanation tonometry. *Optometry and Vision Science*, 85(6):445–450, 2008.

[70] formlabs. Black resin 1 l, 2023. Last accessed 22 May, 2023.

[71] formlabs. Clear resin 1 l, 2023. Last accessed 22 May, 2023.

[72] J Blaber, B Adair, and Antonia Antoniou. Ncorr: open-source 2d digital image correlation matlab software. *Experimental Mechanics*, 55(6):1105–1122, 2015.

[73] V Nežerka. Ncorr_post: Dic post-processing tool. *[Online]. Dostupné: http://mech. fsv. cvut. cz/˜ nezerka/dic/index. htm*, 2014.

[74] Jun Liu and Cynthia J Roberts. Influence of corneal biomechanical properties on intraocular pressure measurement: quantitative analysis. *Journal of Cataract & Refractive Surgery*, 31(1):146–155, 2005.

[75] Xiao Qin, Lei Tian, Haixia Zhang, Xinyan Chen, and Lin Li. Evaluation of corneal elastic modulus based on corneal visualization scheimpflug technology. *BioMedical Engineering OnLine*, 18:1–16, 2019.

[76] Shawna Gloe, Abby Rothering, Julie A Kiland, and Gillian J McLellan. Validation of the icare® tonovet plus rebound tonometer in normal rabbit eyes. *Experimental eye research*, 185:107698, 2019.

[77] Hong Zhang, Dong Yang, Craig M Ross, Jonathan P Wigg, Surinder Pandav, and Jonathan G Crowston. Validation of rebound tonometry for intraocular pressure measurement in the rabbit. *Experimental eye research*, 121:86–93, 2014.

[78] Nur Raihan Razman, Wan Mahani Hafizah Wan Mahmud, and Nurul Aimi Shaharuddin. Filtering technique in ultrasound for kidney, liver and pancreas image using matlab. In *2015 IEEE Student Conference on Research and Development (SCOReD)*, pages 402–406, 2015.